# High-Temperature Strain Localization and the Nucleation of Oceanic Core Complexes (16.5°N, Mid-Atlantic Ridge)

Leonardo Casini, Matteo Maino, Alessio Sanfilippo, Benoit Ildefonse, Henry J B Dick

▶ To cite this version:

Leonardo Casini, Matteo Maino, Alessio Sanfilippo, Benoit Ildefonse, Henry J B Dick. High-Temperature Strain Localization and the Nucleation of Oceanic Core Complexes (16.5°N, Mid-Atlantic Ridge). Journal of Geophysical Research : Solid Earth, 2021, 126 (9), pp.e2021JB022215. ⟨10.1029/2021jb022215⟩. ⟨hal-03343954⟩

HAL Id: hal-03343954
https://hal.science/hal-03343954v1

Submitted on 14 Sep 2021

JGR Solid Earth

RESEARCH ARTICLE
10.1029/2021JB022215

**Special Section:**
Ophiolites and Oceanic Lithosphere, with a focus on the Samail ophiolite in Oman

**Key Points:**

- Troctolites dredged from a detachment fault at the Mid Atlantic Ridge, 16°N preserve a narrow HT shear zone
- Localization at high temperature close to solidus conditions is accommodated by switching from dislocation creep to Grain Boundary Sliding
- Selective remelting of magmatic amphibole triggers Grain Boundary Sliding

**Supporting Information:**

Supporting Information may be found in the online version of this article.

**Correspondence to:**
L. Casini,
casini@uniss.it

**Citation:**
Casini, L., Maino, M., Sanfilippo, A., Ildefonse, B., & Dick, H. J. B. (2021). High-temperature strain localization and the nucleation of Oceanic Core Complexes (16.5°N, Mid-Atlantic Ridge). *Journal of Geophysical Research: Solid Earth*, *126*, e2021JB022215. https://doi.org/10.1029/2021JB022215

Received 9 APR 2021
Accepted 18 AUG 2021

# High-Temperature Strain Localization and the Nucleation of Oceanic Core Complexes (16.5°N, Mid-Atlantic Ridge)

**Leonardo Casini**[1], **Matteo Maino**[2,3], **Alessio Sanfilippo**[2,3], **Benoit Ildefonse**[4], and **Henry J. B. Dick**[5]

[1]Dipartimento di Chimica e Farmacia, Università di Sassari, Sassari, Italy, [2]Dipartimento di Scienze della Terra e dell'Ambiente, Università di Pavia, Pavia, Italy, [3]CNR-IGG, Istituto Geoscienze e Georisorse, Pavia, Italy, [4]Géosciences Montpellier, Université de Montpellier, CNRS, Montpellier, France, [5]Woods Hole Oceanographic Institution, Woods Hole, MA, USA

**Abstract** Extension at slow to ultraslow midoceanic ridges is mostly accommodated by large detachment faults that expose mantle peridotite and/or lower-crustal rocks forming Oceanic Core Complexes (OCC). It is commonly accepted that OCC at slow spreading ridges form during the early stage of crystallization of the magmatic crust, when rocks are still close to their solidus temperature. This observation poses significant problems, as nucleation of detachment faults requires significant weakening, which instead is more easily obtained at low temperature. The RV Knorr cruise 210 Leg 5 on the 16.5°N OCC of the Mid-Atlantic Ridge recovered a narrow shear zone from the plutonic footwall of a mature detachment fault. Troctolites preserve a continuous transition from proto-mylonite to mylonite and ultra-mylonite equilibrated at temperature between 1100° and 900°C. EBSD analysis highlights increased phase mixing and weaker crystallographic fabrics in the ultra-mylonite with respect the mylonitic domains. While host troctolites were completely solidified at the deformation incoming, high-strain zones preserve evidences of syn-kinematic melt-related textures. Fabric patterns combined with plagioclase and olivine grain size piezometry and 1D rheological modeling indicate that the development of ultra-mylonite requires a switch from dislocation creep to melt-enhanced grain-boundary sliding. Activation of this mechanism was promoted by the occurrence of hydrous melt possibly produced by selective re-melting of plagioclase + Ti-pargasite microdomains in response to strain localization at subseismic strain rates. This study highlights the importance of hydrated magmatic phases to promote the onset of detachment faulting in OCC.

**Plain Language Summary** Midoceanic ridges expose the deepest part of the crust and the mantle in dome-like structures called Oceanic Core Complexes. These structures form by extreme crustal extension accommodated by large faults, soon after crystallization of the magmatic crust. This observation rises significant problems, as high temperatures generally promote ductile deformation of the rocks, not faulting and brittle deformation. The RV Knorr cruise 210 Leg 5 on the 16.5°N OCC of the Mid-Atlantic Ridge recovered a mature fault zone deforming mafic rocks defined as amphibole-bearing troctolite. The rocks show a gradient of deformation marked by a progressive decrease of grain size and increasing mixing of different minerals, which become maximum in a narrow 1-cm-thick band. Numerical simulations successfully replicate the microstructure observed in the most deformed zone only assuming very high velocity close to seismic rates. We argue that the presence of a small fraction of intergranular melt derived from selective melting of amphibole and plagioclase served as tectonic lubricant promoting fast deformation and localization at high temperature. The results of this study highlights the importance of amphibole, and possibly other hydrated magmatic minerals, to localize deformation, ultimately yielding to crustal extension and formation of the oceans.

## 1. Introduction

Strain localization plays a major role for the development of shear zones, finally controlling the behavior of plate tectonics. In a simplified physical model, the evolution of shear zones responds to a viscous constitutive relationship between stress ($\sigma$) and strain rate ($\dot{\epsilon}$) that might be expressed as:

$$\sigma = 2\eta\left(\Theta, \dot{\varepsilon}\right)\dot{\varepsilon} \tag{1}$$

where $\eta$ is viscosity and $\Theta$ is a generic rate- and state-dependent variable incorporating the effect of temperature, void/solid fraction, grain-size, rock composition, crystallographic preferred orientation (CPO), or a combination thereof (Bercovici & Karato, 2002). In order to localize shear, $\Theta$ or $\dot{\epsilon}$ should vary to result in a nonmonotonic stress-strain rate relationship. At high temperature ($T > 0.5\ T_\mathrm{m}$ where $T_\mathrm{m}$ is melting temperature), the reduction of grain size may enhance a large decrease of effective viscosity in most rocks, enabling weakening. This, in turn, promotes strain localization and further grain-size reduction, developing a self-amplifying process that stabilizes the shear zone (e.g., Handy et al., 1999; Platt & Behr, 2011). One of the possible critical consequences of grain-size reduction and strain localization is the transition from dislocation creep to diffusion creep (e.g., Miranda et al., 2016; Précigout et al., 2007; Svahnberg & Piazolo, 2010). These two end-member mechanisms ideally switch one to another through grain boundary sliding (GBS) in which strain rate depends nonlinearly on stress and on grain-size (Langdon, 2006). GBS is typically associated with a drop in effective viscosity of several orders of magnitude yielding to strain localization (Drury & Humphreys, 1988; Précigout et al., 2007). GBS is promoted by small grain size, high stress, high strain rates, phase mixing, "easy-slip" CPO arrangements, and intergranular fluids (e.g., Menegon et al., 2015; Platt, 2015). Several studies describe the transition between the different creep regimes in Olivine; however, very few investigate the effectiveness of GBS in plagioclase or in polymineralic aggregates (Jiang et al., 2000; Miranda et al., 2016; Svahnberg & Piazolo, 2010). Furthermore, these studies assume the transition between dislocation creep to GBS to occur at relatively low temperatures ($T < 800$°C), because of grain size reduction after prolonged dislocation creep. Hydrous conditions, as a consequence of injection of seawater-derived fluids within the deformed assemblage, may further facilitate the development of granular flow (e.g., Jöns et al., 2009). GBS, however, can be also activated in presence of partially molten rocks, being thereby able to promote localization and the development of shear zones at hypersolidus conditions (Gardner et al., 2020; Rutter, 1997; Walte et al., 2005).

Since their discovery at the Mid Atlantic Ridge, Oceanic Core Complexes (OCC) at slow-spreading ridges offered the opportunity to recover a large amount of high-temperature shear zones developed in the footwall of long-lived normal faults. Here, high-temperature shearing is thought to initiate detachment faulting soon after crystallization of the oceanic crust (e.g., Dick et al., 2000; Ildefonse et al., 2007; Miranda & John, 2010). Inception of strain localization is mainly attributed to GBS-mediated switch from early diffusion creep at high temperature to localized semi-brittle deformation at sub-solidus conditions (Mehl & Hirth, 2008; Schroeder & John, 2004). The role of low-temperature fluids and/or high-temperature melts in promoting this process is well described in the Atlantis Bank (Southwest Indian Ridge) and related to (a) infiltration of seawater-derived fluids, (b) occurrence of intergranular melts, and (c) formation of late-stage magmatic veins (e.g., Gardner et al., 2020; Ma et al., 2020; Taufner et al., 2021).

In this paper, we document a localization process developed at high-temperature conditions along the 16.5°N OCC of the Mid-Atlantic Ridge. Here, the RV Knorr cruise 210 Leg 5 recovered lower crustal rocks from a long-lived detachment fault system (Figure 1a). Approximately 40% of gabbros show an intense crystal-plastic fabric, developed at high-temperature conditions (900°–1100°C; Sanfilippo et al., 2019). Amongst these samples, one troctolite preserves the transition from a proto-mylonite to mylonite to ultra-mylonite, with the latter forming a microstructural domain distinct in mineralogy and mineral chemistry (Figure 1b). This ultra-mylonite layer reveals plagioclase-amphibole equilibration temperature of about 900°C–1000°C, thus representing a snapshot of the very early stage of nucleation of a crustal shear zone in an OCC. Here, we investigate the deformation mechanisms operative in this decimeter-scale shear zone by combining high-resolution EBSD analyses with simple 1D rheological modeling. The results are used to discuss the changes of texture and the microstructural adjustments yielding to weakening processes. Our findings implicate a key role played by magmatic hydrous phases (Ti-pargasite) in promoting strain localization at the onset of detachment faulting.

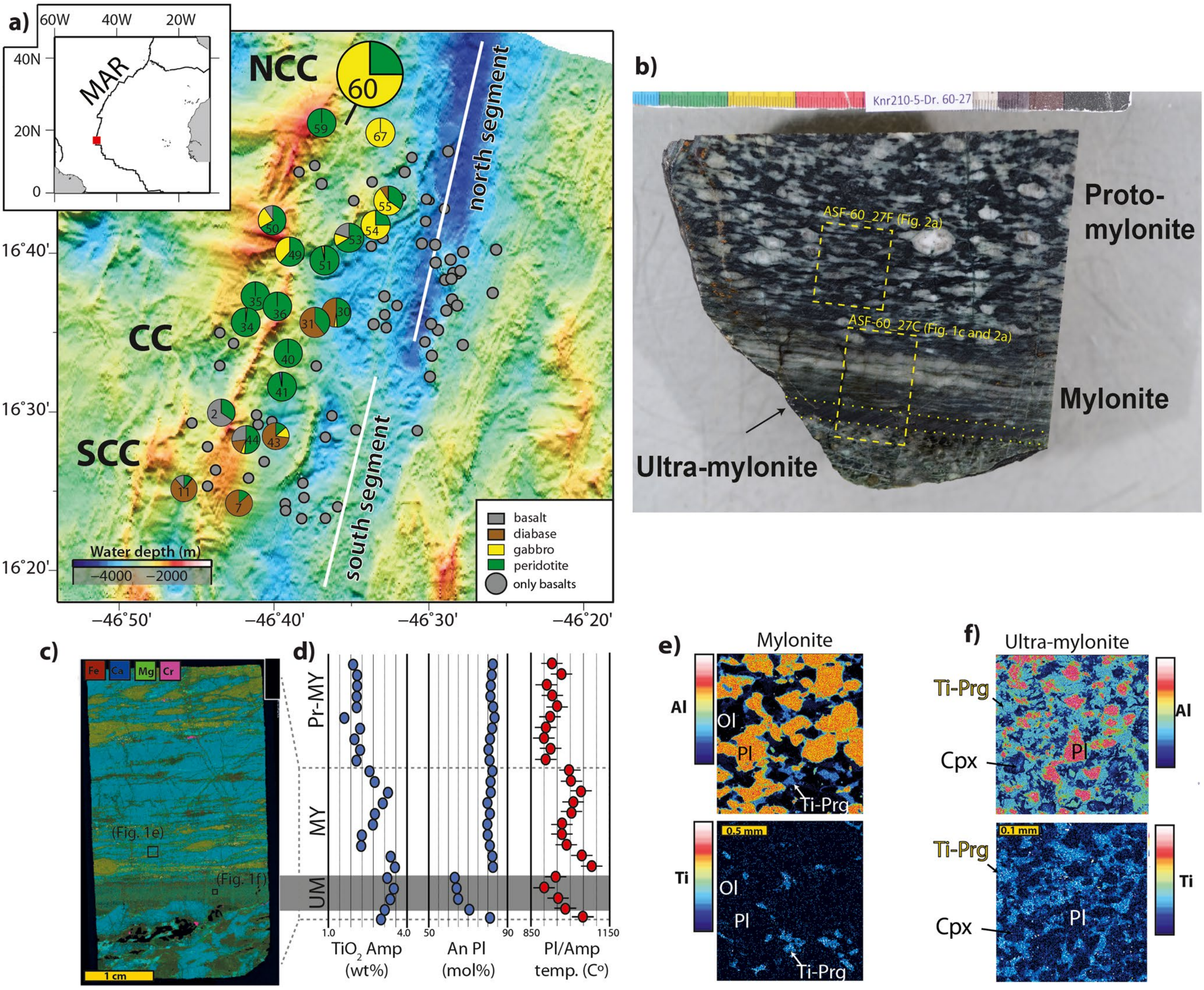

**Figure 1.** (a) Simplified geological map of the 16.5°N Oceanic Core Complexes; NCC Northern Core Complexes, CC Core Complexes, SCC Southern Core Complexes (modified after Sanfilippo et al., 2019). Summary of geochemical data and plagioclase-amphibole thermometry: (b) Photograph of cut hand specimens of the studied troctolite showing a deformation gradient from protomylonite to mylonite and ultra-mylonite. Locations of the thin sections are indicated. (c) Fe, Ca, Mg and Cr element map of mylonite and ultra-mylonite; (d) $TiO_2$ content (amphibole) and An content (plagioclase) variation in plagioclase-amphibole pairs used for thermometric calculations; black bars indicate the uncertainty intrinsic of the method (±40°C; Holland & Blundy, 1994). Element maps of Al and Ti in mylonite (e) and ultra-mylonite (f).

## 2. Geological Background

### 2.1. Structural Setting and Samples Description

The 16°N–17°N region of the Mid Atlantic Ridge includes two spreading segments striking at ~N012° (Figure 1a). The average spreading rate near the 16.5°N OCC is 21.5 mm/yr (Parnell-Turner et al., 2016) and it is accommodated mainly by slip on relatively narrow detachment faults (Escartín et al., 2008). The axis is characterized by a well-developed neo-volcanic zone that is seismically active (Smith et al., 2003). The western side of the rift axis has been identified as a region of active detachment faulting that led to the development of several small-scale OCC's (Escartín et al., 2008). Unlike the thick gabbroic sections exposed in other OCC's such as the Mid Atlantic Ridge or Atlantis Bank in the South West Indian Ridge (SWIR), the OCC's identified in the 16.5°N Mid Atlantic Ridge region are formed by scattered gabbroic intrusions within a partly serpentinized mantle, and therefore likely developed in a magma-poor regime (Parnell-Turner et al., 2016; Sanfilippo et al., 2019). Based on the occurrence of corrugated surfaces, different OCC's were identified, namely the Southern, the Central and the Northern Core Complexes (Smith et al., 2014). Dredging along the footwall of the detachment faults recovered basalts, diabases, and peridotites, whereas gabbroic rocks are rare in the region. Primitive troctolites to minor oxide-gabbro were nonetheless collected at the northern core complex and surrounding areas.

Shipboard observation estimated that nearly 40% of the gabbroic samples preserve textures indicative of shearing and recrystallization under hyper- to subsolidus conditions. Based on plagioclase-amphibole and two-pyroxene thermometry, Sanfilippo et al. (2019) inferred that the development of the porphyroclastic to mylonitic fabrics occurred between 1050°C and 900°C, nearly coincident with the temperatures evaluated in the weakly deformed troctolites (1040 ± 20°C), and close to the solidus temperature of pargasitic amphibole within a mafic assemblage (1020°C; Koepke et al., 2007). The deformation process was likely associated with the local expulsion of interstitial, evolved melts from the crystal matrix. This high-temperature deformation event was then followed by a retrograde metamorphic evolution revealed by the formation of hornblende-rich veins oriented at high angle to the metamorphic foliation and formed at temperatures <750°C. The magmatic assemblage was later replaced by green hornblende and albitic plagioclase at greenschist facies conditions.

A peculiar feature of the gabbros in this region is that strong crystal-plastic deformation features are equally recorded by primitive and evolved lithologies, whereas in some occurrences troctolites are less deformed to undeformed (e.g., Dick et al., 2000). In particular, strongly deformed troctolites were collected in association with dunites and peridotites in the northern OCC, thereby likely representing the plutonic foundations of a gabbroic sequence exhumed by detachment faulting. On this basis, Sanfilippo et al. (2019) interpreted the high-temperature deformation fabric in these rocks as the deep expression of detachment faults. In the present study, we focus on a decimeter-scale shear zone developed on one troctolite collected by dredge KNR210-5-60 on the northeast-facing wall of a crescent shaped ridge crest representing the breakaway zone of a small core complex flanking the rift valley (Figure 1a). The microstructural analysis, along with major element mineral compositions is summarized from Sanfilippo et al. (2019).

### 2.2. Microstructure and Mineral Chemistry

The shear zone shows heterogeneous deformation with intensity increasing progressively from a proto-mylonitic domain, to mylonitic and ultra-mylonitic domains (Figures 1b and 2a). Weakly deformed troctolites bounding the shear zone preserve igneous texture and consist of large, subhedral olivine (forsterite ~88 mol%) and plagioclase ($An_{81}$ in nearly cotectic proportions, 2:3). Accessory phases are represented by interstitial high-Mg# clinopyroxene (Mg# = 100*Mg/[Mg + Fe] = 89), Ti-rich pargasite (Ti-pargasite, $TiO_2$ 4–5 wt.%), Cr-Spinel, and rare interstitial to coronitic orthopyroxene. One remarkable feature of the Mid Atlantic Ridge 16.5°N troctolites is that both clinopyroxene and Ti-pargasite locally occur as large (up to 5 mm) poikilitic grains, enclosing partly corroded, subrounded plagioclase chadacrysts, to form mm-scale clinopyroxene-plagioclase or Ti-pargasite-plagioclase micro-domains randomly distributed in the troctolite matrix (Figure 2b). Proto-mylonite and mylonite have the same mineralogical composition as their troctolite protolith, but show progressively stronger core and mantle structure where large plagioclase and olivine porphyroclasts (up to a few mm) are surrounded by a fine-grained recrystallized matrix composed of plagioclase, olivine with minor clinopyroxene, Ti-pargasite and orthopyroxene (Figures 1b, 2a, 2c, 2d, 3a, 3b, 4a, and 4b). The chemical composition of the recrystallized neoblasts is roughly similar to that of the porphyroclasts, although we note slightly lower anorthite contents in plagioclase neoblasts compared to the porphyroclasts, having $An_{78}$ and $An_{82}$ mol.%, respectively.

Clinopyroxene and orthopyroxene are found as fractured porphyroclasts almost devoid of lattice strain (Figures 4a, 4b, and 5a; see also the large maps provided in the Supporting Information S1). On the contrary, plagioclase and olivine porphyroclasts show microstructural evidence of intracrystalline deformation, such as tapering twins, undulose extinction and straight to slightly curved subgrain boundary walls (Figures 2c, 2d, 4a, and 4b). The size of subgrains is similar or slightly larger than the size of recrystallized grains, suggesting little annealing. Plagioclase porphyroclasts locally form highly strained monomineralic ribbons characterized by nearly equant grains of similar size (Figures 4a and 4b). Recrystallized grains are either slightly elongate, with straight grain boundaries oriented at low angle to foliation, or more equant

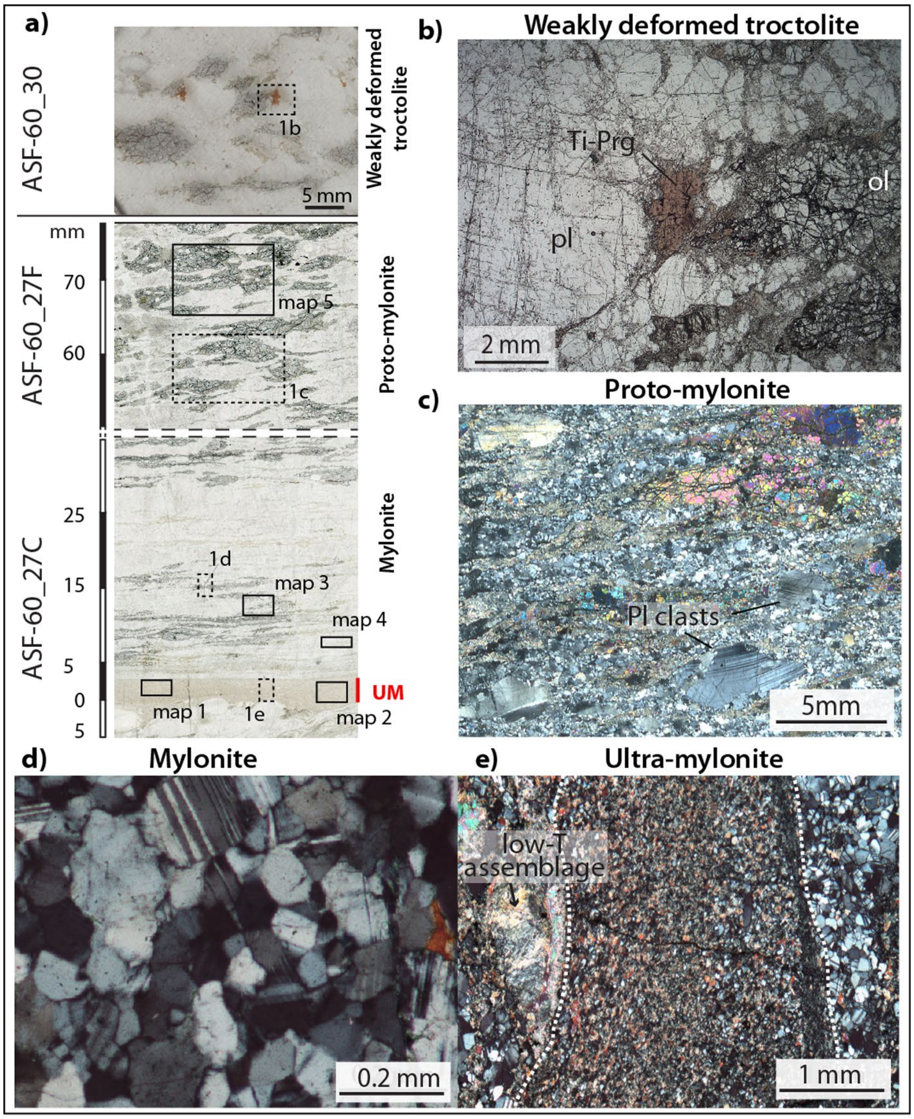

**Figure 2.** Plane polarized (a–c) and crossed polarized (d and e) light thin section photomicrographs: (a) microstructure of weakly deformed, proto-mylonite, mylonite, and ultra-mylonite domains; the position of EBSD maps is indicated by solid squares; (b) primary olivine (Ol) + plagioclase (Pl) + clinopyroxene assemblage in troctolite with a detail of mm-size primary Ti-Pargasite (Ti-Prg); (c) close-up of proto-mylonite with plagioclase porphyroclasts mantled by fine-grained recrystallized matrix; (d) nearly monomineralic plagioclase layer in mylonite; (e) microstructure of the Ti-pargasite-plagioclase ultra-mylonitic band; the dotted line marks the boundary of the high-strain zone.

(Figures 4a, 4b, 5c, and 5d). Abundant four-grain junctions and alignment of straight grain boundaries appear throughout the recrystallized matrix (Figure 5d).

Outside the ultra-mylonite, amphiboles are rare and found exclusively as small grains mixed in the neoblastic matrix surrounding olivine or plagioclase porphyroclasts (Figures 4a, 4b, 5a, and 5b). They have pargasitic composition, locally showing somewhat lower Ti contents ($TiO_2$ 4–2 wt%) with respect to the accessory Ti-pargasite in the undeformed troctolites (Figures 1d–1f). Noticeably, Ti-pargasite in mylonitic domains shows widespread microstructures indicative of syn-tectonic crystallization. These textures include thin films and inclusion trails preserved within plagioclase grains, and cuspate-lobate morphologies, and clearly suggest that amphibole crystallized from melts present during the deformation event (Figures 3a and 3b).

The 7–15 mm-thick ultra-mylonite (Figures 1b and 2a, e) shows a distinct mineralogical composition mostly made of Ti-pargasite (∼65 vol%) and plagioclase (∼30 vol%). Minor clinopyroxene (<1 vol%) is also present,

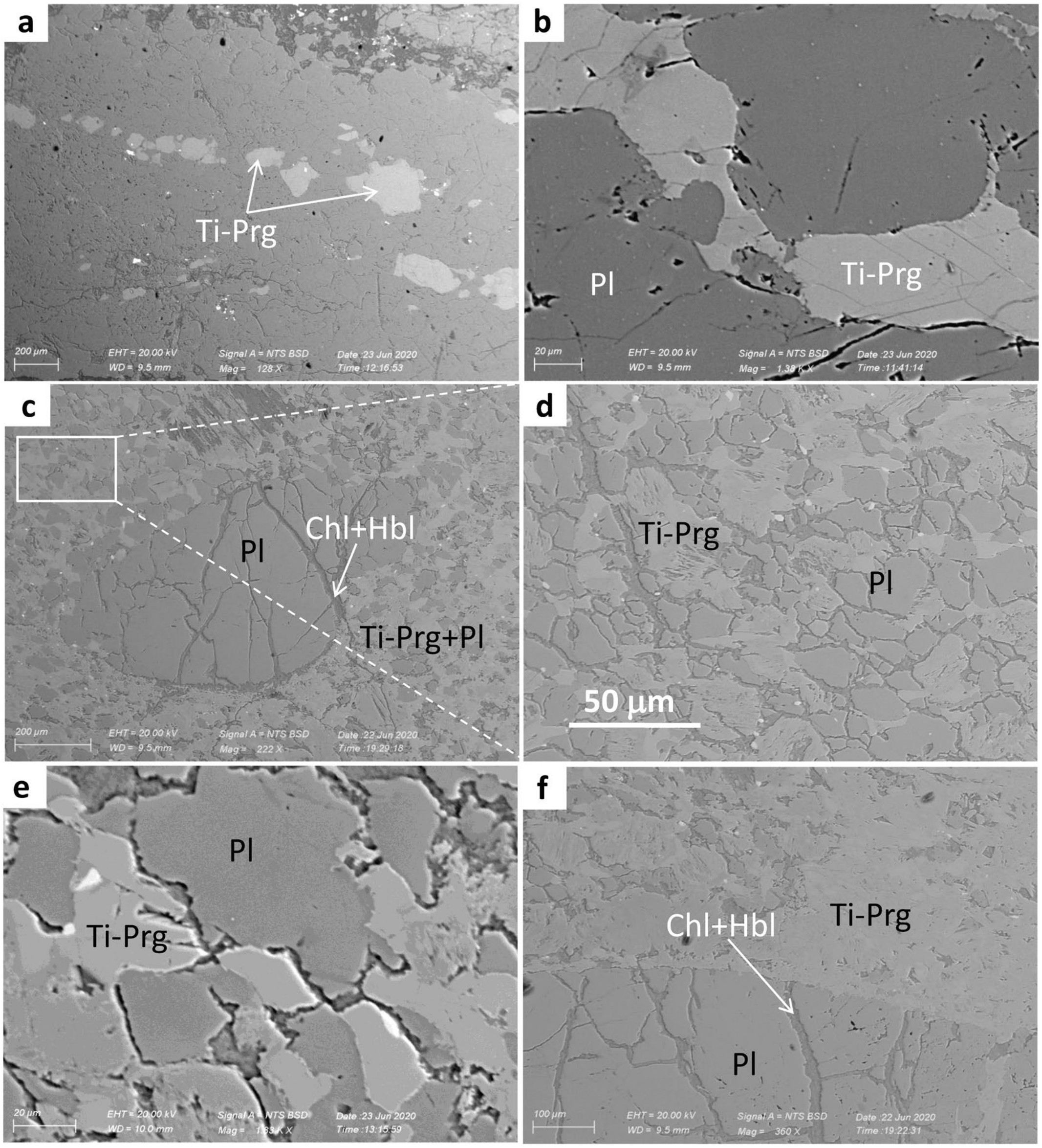

**Figure 3.** Representative microstructure in backscatter electron images: (a) inclusion trails of Ti-pargasite (Ti-Prg) within plagioclase (Pl) from the mylonite; (b) interstitial Ti-pargasite within plagioclase grain boundaries, from the mylonite; (c) ultra-mylonite domain with relic plagioclase porphyroclasts. The fractures in plagioclase are filled by a crypto-crystalline matrix of chlorite + green hornblende (Chl + Hbl); (d) close-up of the fine grained domain of the ultra-mylonite; (e) detail of two four-grain boundary junctions, ultra-mylonite; (f) transition between a plagioclase porphyroclast and the fine-grained domain of ultra-mylonite.

locally associated with orthopyroxene (0–3 vol%) (Figure 4c). Remarkably, olivine and Cr-Spinel are absent, as well as Ti-Fe oxides. Both plagioclase and Ti-pargasite are generally characterized by very fine grainsize (<10 μm), although some larger plagioclase porphyroclasts (up to ~30 μm) are randomly preserved (Figures 3c and 5e). Ti-pargasite has subhedral habits, and show optically continuous thin films extending between the plagioclase grain boundaries. The rare plagioclase porphyroclasts are heavily fractured and the fractures are filled by a crypto-crystalline matrix of chlorite + green hornblende (Figures 3c and 3f). Plagioclase and Ti-pargasite grains do not preserve evidence of intracrystalline deformation and are slightly elongated along a main direction forming moderate angle (10°–30°) with respect the ultra-mylonite walls (Figures 4c and 5e). Four-grain junctions are widespread throughout the fine-grained domain (Figures 3e, 5f, and 5g).

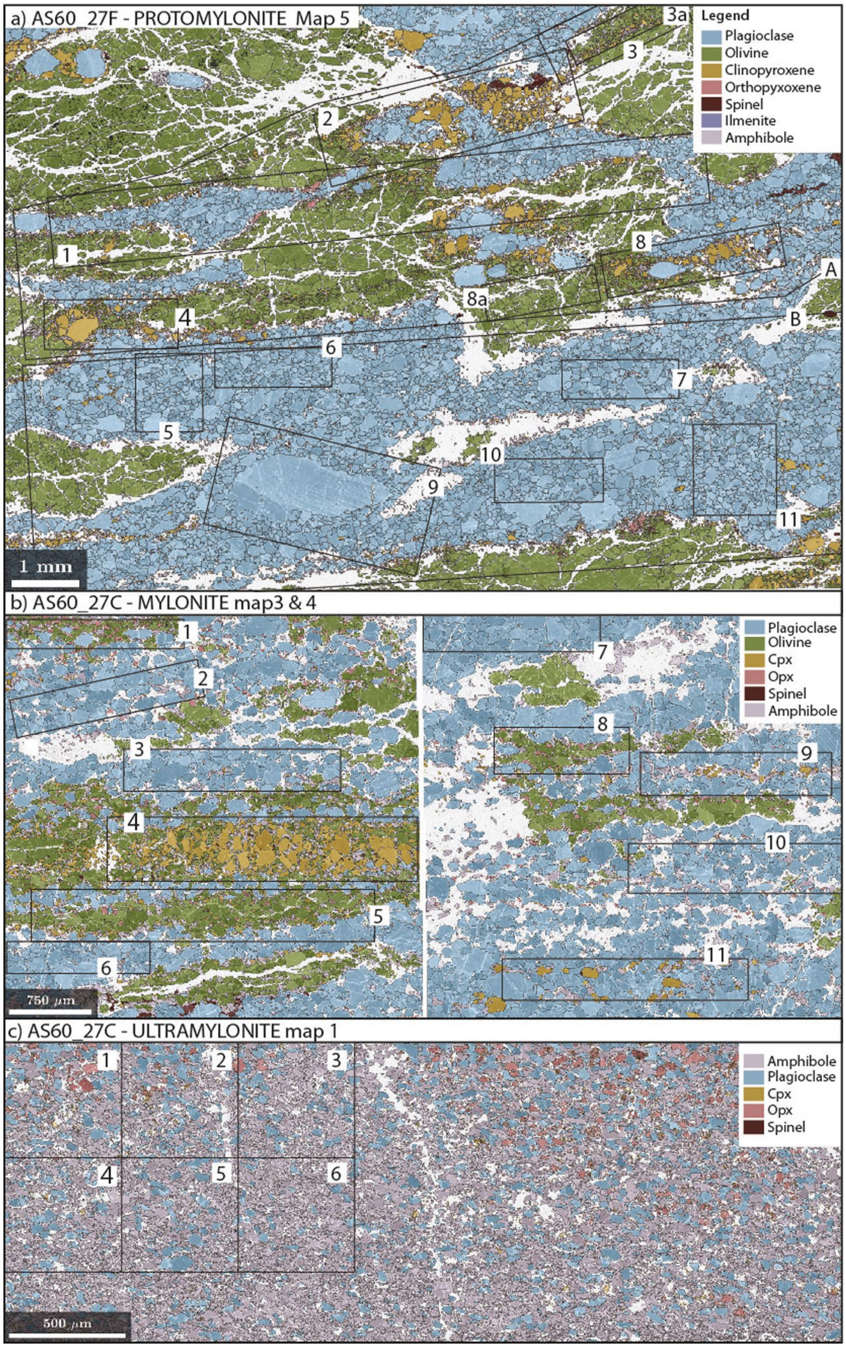

**Figure 4.** EBSD phase distribution and orientation maps of (a) proto-mylonite, (b) mylonite, and (c) ultra-mylonite; the rectangles indicate the subdomains used to calculate the degree of grain size and phase mixing (Table 1). Large size maps are provided in the Supporting Information S1. Cpx and Opx refer to clinopyroxene and orthopyroxene, respectively.

Recrystallized plagioclase in the ultra-mylonite has lower An contents (~65 mol%) compared to that in both the porphyroclasts and neoblasts in the host porphyroclastic and mylonitic domains (An 75–85) (Figures 1c–1f). In contrast, the composition of Ti-pargasite within the ultra-mylonite layer is similar to that in the mylonite and proto-mylonite. The transition from the mylonite to the ultra-mylonite is marked by a straight, subplanar boundary on one side, while the other contact is gradual and partly replaced by a seam of fine-grained green hornblende associated with albite and chlorite statically replacing the pre-existing

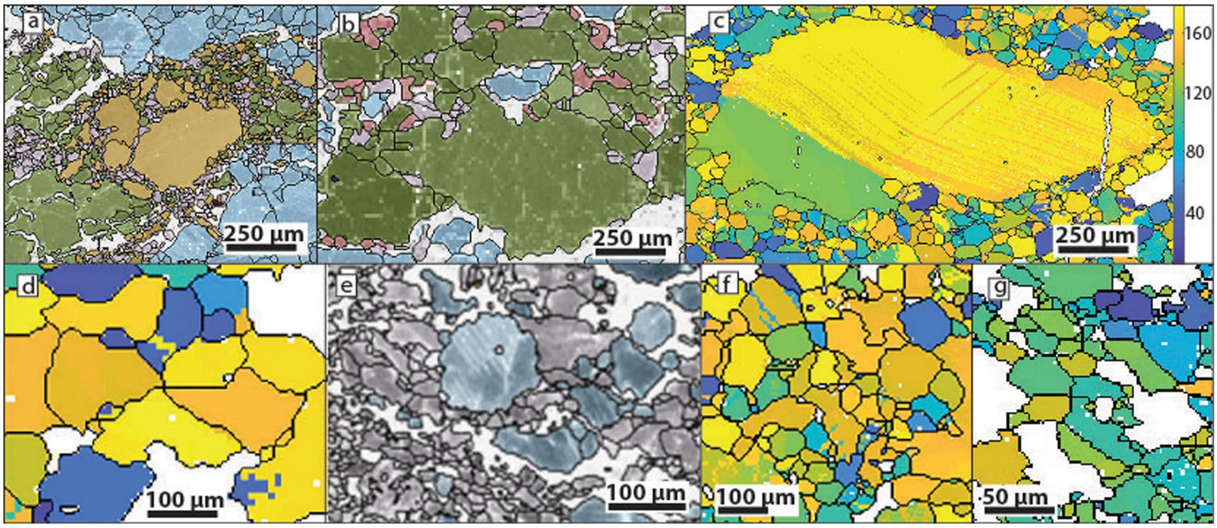

**Figure 5.** Representative microstructures of (a–d) proto-mylonite/mylonite, and (e–g) ultra-mylonite domains. Colors of (a), (b), and (e) are the same as Figure 4, whereas the color bar of (c) describe the 0°–180° orientation of grain boundaries in (c and d) and (f and g) (see the Supporting Information S1 for the complete maps). (a–c) porphyroclasts of clinopyroxene, olivine and plagioclase surrounded by fine grained recrystallized matrix. (d) four-grain junction in plagioclase from the mylonite matrix. (e) strained plagioclase porphyroclasts dispersed in a fine-grained matrix dominated by Ti-pargasite. (f and g) Ti-pargasite grains show four-grain junction in the ultra-mylonite domain.

phases (Figure 2e). The latter represents alteration products due to the ingress of seawater at amphibolite to upper green-schist facies conditions (see Sanfilippo et al., 2019).

## 3. Methods

Temperatures of plagioclase and Ti-pargasite couples were estimated using the plagioclase-amphibole thermometer of Holland and Blundy (1994), calculated at pressure of 0.2 GPa, which corresponds to about ~6–7 km of depth under the assumption of lithostatic pressure. The relative temperature uncertainty is stated as ±40°C in a wide temperature and pressure range matching the conditions recorded by troctolite (Holland & Blundy, 1994).

Microstructural and crystallographic data, CPO and shape preferred orientation (SPO) for olivine, plagioclase, clinopyroxene, orthopyroxene, and amphibole-were collected using SEM-EBSD on areas representative of the ultramylonite (maps 1 and 2), mylonite (maps 3 and 4), and proto-mylonite (map 5) domains (Figure 2a). Although Ti-pargasite is largely dominant, we use the more generic label "amphibole" because the EBSD analyses do not allow distinguishing amphiboles with different chemical composition. A full description of the analytical procedures and the large size maps are available in the Supporting Information S1. The intensity of phase mixing is calculated from the EBSD maps following the procedure described in Appendix A. Finally, the relationships among deformation mechanisms, grain size, stress, and strain-rate at various temperature conditions have been investigated by calculating stress and strain-rate temperature profiles for a composite made of olivine + plagioclase + pyroxene + amphibole in modal proportions matching those of troctolite, as described in Appendix B.

## 4. Results

### 4.1. Thermometry

Plagioclase rims and adjacent Ti-Pargasite in the weakly deformed troctolites preserve magmatic texture and have been used to infer the crystallization temperature of the late-stage melt. In the proto-mylonite, mylonite, and ultra-mylonite domains, plagioclase and Ti-pargasite show microstructural features indicative of chemical equilibration during deformation and recrystallization, thus providing the opportunity to estimate the deformation temperature. The resulting equilibrium temperatures range from 1060°

to 1020°C for the weakly deformed troctolite, 900°C–975°C for the proto-mylonite, 950°–1100°C for the mylonite, and ~900°–1000°C for the ultra-mylonite (Figure 1d). A traverse roughly perpendicular to the protomylonite-mylonite-ultramylonite contacts show a gradual increase of the temperature estimates for plagioclase-amphibole pairs, without any apparent lateral variability at the thin section scale (Figure 1d). The higher temperature were found at the contact between the mylonite and the ultra-mylonite. Here, amphibole-plagioclase temperatures decrease from ~1000 °C to ~900°C toward the central portion of the ultra-mylonite layer (Figure 1d). Although these estimates are subjected to the uncertainty intrinsic of the thermometric method (±40°C), the gradient in temperature is sustained by a systematic increase in $TiO_2$ contents of the Ti-pargasite that show a gradually increase from the neoblastic domains in the proto-mylonite (1.5 wt%) toward the mylonite/ultra-mylonite boundary (3.5 wt%).

### 4.2. Shape Preferred Orientation (SPO) Data

Plagioclase porphyroclasts are equant to slightly elongated (average axial ratio of 1.5) with a weak shape preferred orientation at low angle (~10°–15°) with respect to the mylonitic foliation. The plagioclase neoblasts in the proto-mylonite and mylonite display an average aspect ratio of 1.43–1.47. The aspect ratio rises slightly in the ultra-mylonite domain reaching 1.52–1.54 (Table1). In these domains, plagioclase grains are slightly elongated, with a preferred orientation of particle long axes inclined at ~8°–12° with respect to the foliation plane (Figures 4a and 4b). Amphibole grains show constantly higher aspect ratio and elongation in the proto-mylonite, mylonite (1.50–1.56), and the ultra-mylonite (1.54–1.59) (see Table 1). The shape preferred orientation of both plagioclase and amphibole in ultra-mylonite is well developed, with a mean angle of ~38°to the main mylonitic foliation (Figure 4c).

### 4.3. Misorientation Data

Crystallographic misorientation in plagioclase varies significantly between porphyroclasts and matrix in each map. Neoblasts have systematically low intragrain misorientation with respect to the porphyroclasts, which show significantly higher values (Figure 6). Particularly, the large porphyroclasts from the weakly deformed domains display the highest misorientations (up to 10°) relative to subgrain boundaries (Figures 6a and 6b). The recrystallized matrix in all domains has a mix of strained grains and strain-free grains (Figure 6). The misorientations of neoblastic plagioclase are mainly located at the contact with neighboring grains, suggesting intense proto mylonite intragranular strain in both elongate and equant recrystallized grains.

### 4.4. Crystal-Plastic Orientation (CPO) Data

Olivine in proto-mylonite and mylonite occurs as large isolated crystals, or as incipient monomineralic ribbons apparently derived from single porphyroclasts. Olivine CPO in proto-mylonite is strong and well oriented (Figure 7a) with respect the more dispersed data from the mylonite (Figure 7b). However, the olivine grains of proto-mylonite are fractured due to the serpentinization process, making the olivine CPO statistically insignificant.

Plagioclase CPO in the proto-mylonite (Figure 7a) is relatively weak (J index 2.13 and M index 0.05) but well organized, forming distinct clusters of [100] parallel to the lineation, (010) subparallel to the pole of foliation, and a discontinuous great circle of poles to the (001) plane. The Misorientation Angle Distribution (MAD) of correlated points shows high amplitude frequency peaks at low (<5°) misorientation angles, while the dominant rotation axes cluster close to [100].

The plagioclase CPO in the mylonite is weaker (J index 1.95 and M index 0.03) and shows a reduced organization of the pattern compared to proto-mylonite (Figure 7b). Consistently, the misorientation-angle distribution analysis shows a high amplitude frequency peaks at low angle (<10°), while the misorientation axes cluster around [100].

The dispersion of orientations in plagioclase CPO is somewhat higher in ultra-mylonite (J index 1.95–1.82 and M index 0.03–0.04), but the CPO and misorientation-angle distribution (Figure 7c) remains overall consistent with that of the mylonite, while the misorientation axes cluster around both [100] and the poles to (100).

**Table 1**
*Microstructural and Fabric Data*

| Sample | Layer (see Figure 4) | Composition | Phase | % | Grain size (μm) | Differential stress (MPa) | SPO | CPO strength | | Dist (mm) |
|---|---|---|---|---|---|---|---|---|---|---|
| | | | | | | | | J | M | |
| Protomylonite ASF60_27F | Full map | Poly | Pl | 41 | 43 | | 1.47 | 2.13 | 0.05 | 65–75 |
| | | | Amp | 3.6 | 18 | | 1.56 | 1.39 | 0.04 | 70–75 |
| | A | Poly | Pl | 35 | 43 | | 1.43 | | | 70–75 |
| | B | Poly | Pl | 83 | 48 | *76* | 1.42 | | | 65–70 |
| | 1 | Poly | Pl | 41 | 78 | *78* | 1.44 | | | 70–75 |
| | 2 | Poly | Pl | 30 | 30 | | 1.43 | | | 70–75 |
| | 3 | Poly | Pl | 18 | 31 | | 1.61 | | | 70–75 |
| | 3a | Poly | Ol | 85 | 28 | | | | | 70–75 |
| | 4 | Poly | Pl | 70 | 36 | | 1.48 | | | 70–75 |
| | 5 | Mono | Pl | 100 | 49 | 75 | 1.41 | | | 65–70 |
| | 6 | Mono | Pl | 98 | 45 | 79 | | | | 65–70 |
| | 7 | Mono | Pl | 99 | 45 | 79 | | | | 65–70 |
| | 8 | Poly | Pl | 40 | 32 | | | | | 70–75 |
| | 8a | Mono | Ol | 94 | 38 | *90* | | | | 70–75 |
| | 9 | Mono | Pl | 96 | 45 | 79 | | | | 65–70 |
| | 10 | Mono | Pl | 100 | 50 | 74 | | | | 65–70 |
| | 11 | Mono | Pl | 99 | 47 | 77 | | | | 65–70 |
| Mylonite ASF60_27C_maps3&4 | Full map | Poly | Pl | 50 | 44 | | 1.50 | 1.95 | 0.03 | 10–15 |
| | | | Amp | 7.7 | 18 | | 1.55 | 1.12 | 0.00 | 10–15 |
| | 1 | Poly | Pl | 24 | 29 | | 1.31 | | | 10 |
| | 2 | Mono | Pl | 94 | 48 | 76 | 1.41 | | | 10 |
| | 3 | Poly | Pl | 84 | 45 | *79* | 1.45 | | | 10 |
| | 4 | Poly | Pl | 11 | 33 | | 1.49 | | | 10 |
| | 5 | Poly | Pl | 23 | 37 | | 1.44 | | | 10 |
| | 5 | Poly | Ol | 64 | 26 | | | | | |
| | 6 | Poly | Pl | 96 | 39 | 87 | 1.36 | | | 10 |
| | 7 | Mono | Pl | 100 | 44 | 80 | 1.38 | | | 15 |
| | 8 | Poly | Pl | 2 | 33 | | 1.51 | | | 15 |
| | 9 | Poly | Pl | 66 | 40 | | 1.49 | | | 15 |
| | 10 | Mono | Pl | 90 | 41 | 84 | 1.44 | | | 15 |
| | 11 | Poly | Pl | 79 | 41 | *84* | 1.54 | | | 15 |
| Ultramylonite ASF60_27C_map 1 | Full map | Poly | Pl | 20 | 9.1 | | 1.52 | 1.95 | 0.03 | 0–05 |
| | | | Amp | 53 | 6.7 | | 1.55 | 1.63 | 0.04 | 0–05 |
| | 1 | Poly | Pl | 37 | 9.8 | | 1.59 | | | 0.5 |
| | 2 | Poly | Pl | 34 | 10.4 | | 1.55 | | | 0.5 |
| | 3 | Poly | Pl | 26 | 10.6 | | 1.53 | | | 0.5 |
| | 4 | Poly | Pl | 28 | 7.8 | | 1.49 | | | 0 |
| | 5 | Poly | Pl | 25 | 9.4 | | 1.48 | | | 0 |
| | 6 | Poly | Pl | 13 | 8.4 | | 1.52 | | | 0 |

**Table** *1*
*Continued*

| Sample | Layer (see Figure 4) | Composition | Phase | % | Grain size (μm) | Differential stress (MPa) | SPO | CPO strength J | CPO strength M | Dist (mm) |
|---|---|---|---|---|---|---|---|---|---|---|
| Ultramylonite ASF60_27C_map 2 (see Supporting Information S1) | Full map | Poly | Pl | 20 | 9.0 | | 1.55 | 1.82 | 0.04 | 0 |
| | | | Amp | 54 | 6.8 | | 1.59 | 1.63 | 0.04 | 0 |

*Note*. Layer labels are provided in Figure 4. Map 2 from the ultra-mylonite may be found in the supplementary data set. Composition refers to monophase or polyphase zones. Phase are plagioclase (Pl), olivine (Ol), and amphibole (Amp). Percent is the modal percent of the phase; Differential stresses are estimated only for monophase layers or (in italics) based on the stress estimates of neighbouring monophase layers (where present). Shape preferred orientation (SPO) (where available) is represented as average aspect ratio. *J* and *M* indexes are the quantification of the fabric strength derived from crystallographic preferred orientation (CPO). Dist is the distance from the center of the ultra-mylonite.

Amphibole forms well-developed CPO's in all the structural domains, which decrease in intensity from proto-mylonite (J index 1.39 and M index 0.04) to mylonite (J index 1.12 and M index 0), then increasing in the ultra-mylonite (J index 1.63 and M index 0.04). The amphibole CPO patterns have a distribution of (100) planes parallel to the foliation (XY plane), with the (010) planes lying parallel to the XZ plane, and a strong alignment of [001] poles parallel to the lineation (Figure 7c). The misorientation-angle distribution in the mylonite is close to the theoretical random distribution, with a high frequency of the <10° misorientation angles. The ultra-mylonite shows a larger spread of distribution and significantly lower frequency of small angle values (<10°). The misorientation axes are characterized by a shift of the main cluster from [001] in proto-mylonite and mylonite to the [010] axis in the ultra-mylonite domain. Overall, the amphibole CPO is significantly stronger in the ultra-mylonite compared to the other domains.

### 4.5. Phase Mixing

The spatial analysis of the grain boundary maps extracted from EBSD data combined with the compositional maps allows estimating the degree of phase mixing in the different domains. Overall, the results show a systematic increase of phase mixing which is inversely correlated with the distance from the high-strain ultra-mylonite zone and mean grain size (Supporting Information S1). The proto-mylonite and mylonite domains, in fact, are characterized by low and gently increasing degree of phase mixing ($\mu = 0.02–0.005$ and 0.12–0.01, respectively) whereas the ultra-mylonite layer shows markedly higher values very close to the theoretical maximum ($\mu = 0.99–0.5$). The comparison of normalized $\mu$ values shows that there is no obvious correlation between the number and type of phases coexisting in a microstructural domain and the degree of mixing (Supporting Information S1). Polymineralic layers of proto-mylonite and mylonite (i.e., subsets 2 and 3 of Figure 4a, and subsets 1 and 4 of Figure 4b), indeed, show very low degrees of phase mixing in spite of their variable mineralogical composition and grain-size.

### 4.6. Grain Size Variability

The variation of grain size distribution in the different microstructural domains is estimated from plagioclase and olivine, although the latter is not present in the ultra-mylonite. Plagioclase appears in both mono- and poly-phase layers. In the latter microstructural sites, it may be present either as the volumetrically dominant or subordinate phase (Figure 4). Olivine is generally associated with pyroxene and amphibole and locally it represents the dominant phase in the recrystallized matrix, mantling large olivine porphyroclasts (Figures 4a and 5b). Olivine porphyroclasts are characterized by abundant fractures associated with late serpentinization during low-T re-equilibration, preventing good estimations of their original grain size. The recrystallized olivine-rich mylonitic layers show instead minor evidence of low-temperature alteration offering valid comparison to the adjacent plagioclase-dominated layers.

Table 1 contains the grain-size distribution of plagioclase and olivine in the different domains and subdomains of the shear zone (Figure 4). Excluding the porphyroclasts, the plagioclase grain size outside the ultra-mylonite ranges between ∼120 and 12 μm, with median values of 43–44 μm (Table 1). In particular,

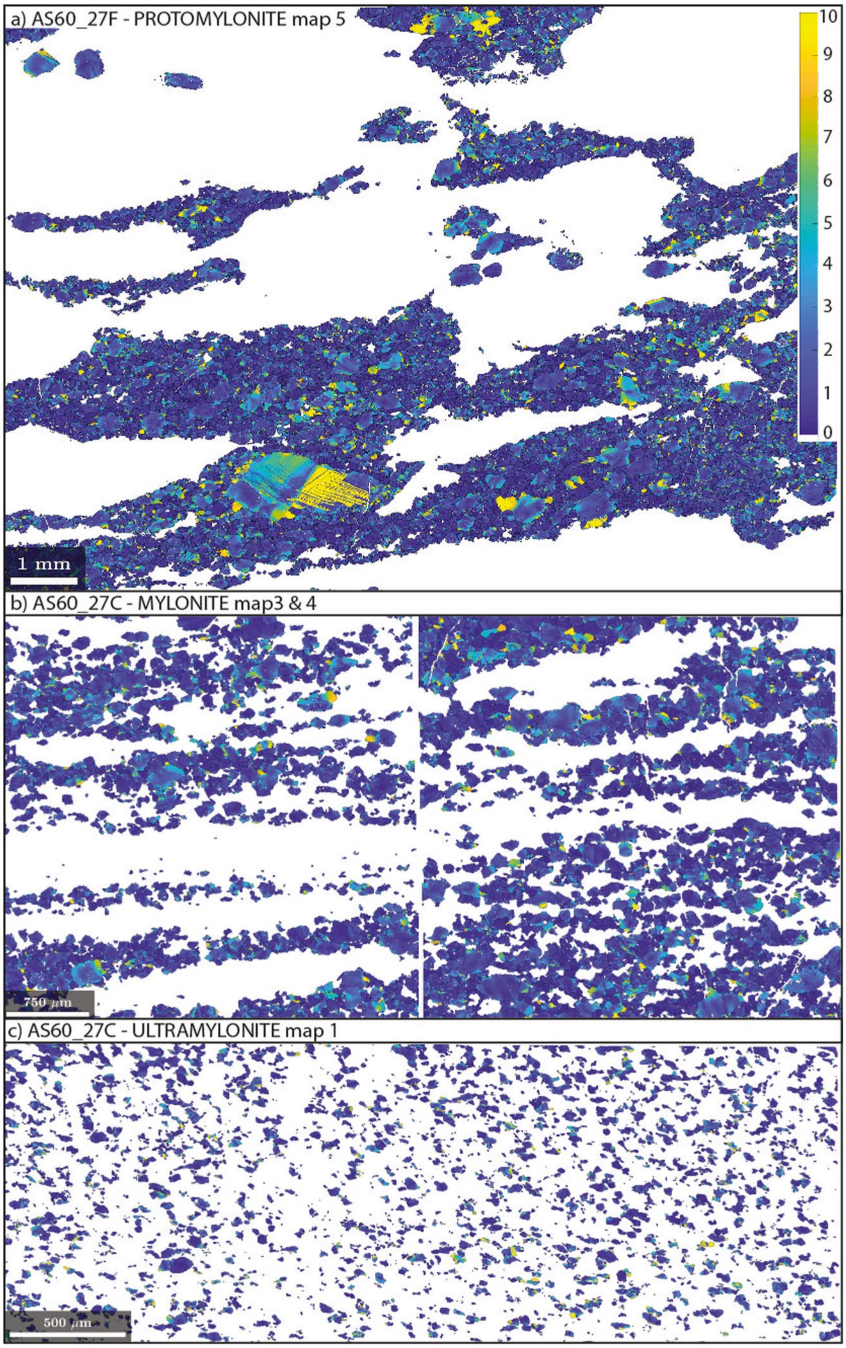

**Figure 6.** Misorientation maps of plagioclase grains from the representative domains of proto-mylonite (see map 5), mylonite (maps 3 and 4), and ultra-mylonite (map 1). Maximum value of misorientation is 10° (yellow) and the minimum is 0°–2° (blue).

the monomineralic layers yield homogeneous values between ∼41 and 50 μm, while the grain size decreases slightly (29–44 μm) in the polymineralic layers, particularly when its volume fraction $\phi_{\mathrm{plagioclase}} < 0.5$ (see Supporting Information S1). In the small subdomains, where the olivine grain size can be estimated, the recrystallized grain size is of the order of 28–38 μm. Amphibole in all domains shows lower grain size, ranging between 15 and 20 μm. To investigate the effect of the presence of other phases on the grain size variability of plagioclase, we analyzed the grain-size variation in the subdomains containing variable fractions of each phase. The mean grain size of olivine, ortho/clinopyroxene and amphibole is systematically

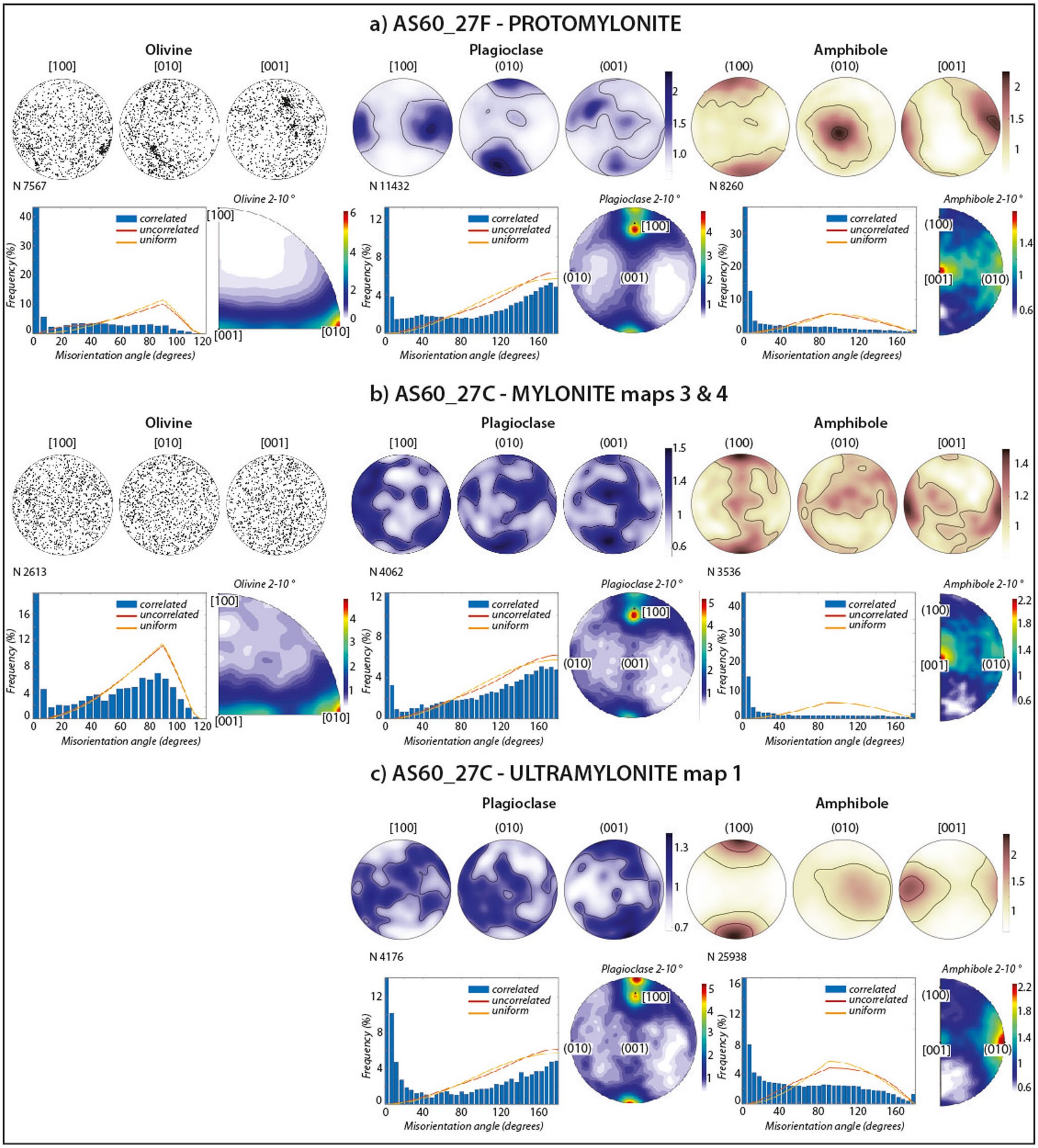

**Figure 7.** Crystallographic preferred orientation (CPO) pattern, misorientation-angle distribution, and rotation axes for the low (2°–15°) misorientation angles in the crystallographic reference frame, for olivine, plagioclase, and amphibole of proto-mylonite, mylonite, and ultra-mylonite. Grain orientations are shown as equal-area, lower hemisphere stereographic projections; *N* is the number of measured grains; and contours for plagioclase and amphibole are multiple of uniform distribution. Misorientation-angle distribution histograms present data for correlated points (angle between neighbor measurement points) compared to the theoretical random distribution. Contours in the inverse pole figures are multiple of uniform distribution.

lower than that of the coexisting plagioclase in plagioclase-rich polymineralic layers. Yet, all phases show a similar grain size when the volume fraction of plagioclase approaches that of the other phases (Supporting Information S1). Second-phase pinning vanishes as the volume fraction of other phases become much lower than that of plagioclase.

A dramatic grain size reduction marks the transition to ultra-mylonite domain, which shows very fine-grained plagioclase (∼7–11 μm) and amphibole (∼6–7 μm).

### 4.7. Evolution of Differential Stress and Strain Rate

In order to investigate the grain size, stress, temperature and strain rate relationships, we calculated stress and strain-rate/T profile for a troctolite composite (see Appendix B). Deformation mechanism maps have been constructed in T/strain-rate space for the main rock-forming minerals such as anorthite, olivine, clinopyroxene and hornblende, given a characteristic grain size corresponding to the median grain size of each mineral species in mylonite (Figure 8). Overall, the topology of the maps is fairly consistent with microstructural observation and petrologic constraints. At $T > 900°\mathrm{C}$, in fact, pyroxene, is expected to be the strongest phase deforming by dislocation-facilitated Rachinger GBS or dislocation creep at very-high strain rates (Figure 8a). Plagioclase and olivine, the main constituent phases of troctolite, are much weaker and deform primarily by diffusion creep or diffusion accommodated Lifshitz GBS at high strain rates (Figure 8a) (Lifshitz, 1963; Langdon, 2006). Amphibole is the weakest phase of the composite showing Newtonian behavior under most temperature and strain-rate conditions (Figure 8a). The strength of the composite troctolite has been calculated using either an homogeneous stress (iso-stress) or homogeneous strain rate (iso-strain) mechanical constraint, respectively (Appendix B). The temperature/stress profiles show that, under the assumption of uniform stress, troctolite requires only about 50 MPa to flow, with a mean strain-rate of $1 \times 10^{-12}$ s$^{-1}$, whereas both plagioclase and olivine taken as single components would require much higher stress >200 MPa (Figure 8b). The strength profiles calculated using the constant strain-rate mechanical constraint show similar results, with the composite still generally weaker than either plagioclase or olivine. In fact, at about 950°C and 80 MPa, the strain rate of troctolite is close to $1 \times 10^{-8}$ s$^{-1}$, whereas pure plagioclase is $7.3 \times 10^{-9}$ s$^{-1}$ and olivine is almost two orders of magnitude stronger (Figure 8c). The rheology of the ultra-mylonite, a bimineralic composite made of variable proportions of amphibole and anorthite, is similar to that of mylonite for >75 vol.% plagioclase compositions (Figure 8d). However, for a composition of 25 vol.% of plagioclase, the strength of ultra-mylonite decreases significantly approaching a theoretical value of $1 \times 10^{-6}$ s$^{-1}$ at about 800°C (Figure 8d). The homogeneous strain rate models are consistent with paleostress estimates provided by plagioclase and olivine piezometers (Mehl & Hirth, 2008; Twiss, 1977) (Figures 8c and 8d). Plagioclase layers record a relatively narrow range of stress values between about 70 and 80 MPa in the proto-mylonite and mylonite, whereas in ultra-mylonite they record much higher stress values, mostly above 200 MPa (Figure 8c). Olivine roughly confirms this general behavior though a slight shift toward higher stress values can be observed (Figure 8c).

## 5. Discussion

### 5.1. Interpretation of CPO Patterns

The plagioclase CPO in the proto-mylonite domain is consistent with deformation dominated by slip on the (010) planes, and defined by a preferred alignment of [100] axis. In turn, the misorientation data indicates that the main rotation axis for misorientation is [100] (Figure 7), which is not compatible with activation of the (010) [100] or (001) [100] slip systems. These observations suggest that plagioclase CPO in the proto-mylonite might reflect inheritance of a magmatic flow fabric as typically observed in gabbros from oceanic crust (e.g., Satsukawa et al., 2013), and/or results from the activation of multiple slip systems (Allard et al., 2020). Plagioclase CPO's in the mylonite and, particularly in the ultra-mylonite, show lower degree of crystallographic orientations, indicating that grain-size reduction was accompanied by randomization of the plagioclase pattern. The progressive loss of plagioclase CPO may be due to destruction of the pre-existing fabric by incipient dislocation creep on [100] (010) or [100] (001) slip systems. Alternatively, the decrease of plagioclase CPO intensity in the ultra-mylonite zone might be interpreted in terms of a switch from dislocation creep-accommodated deformation to diffusion-accommodated grain-boundary sliding

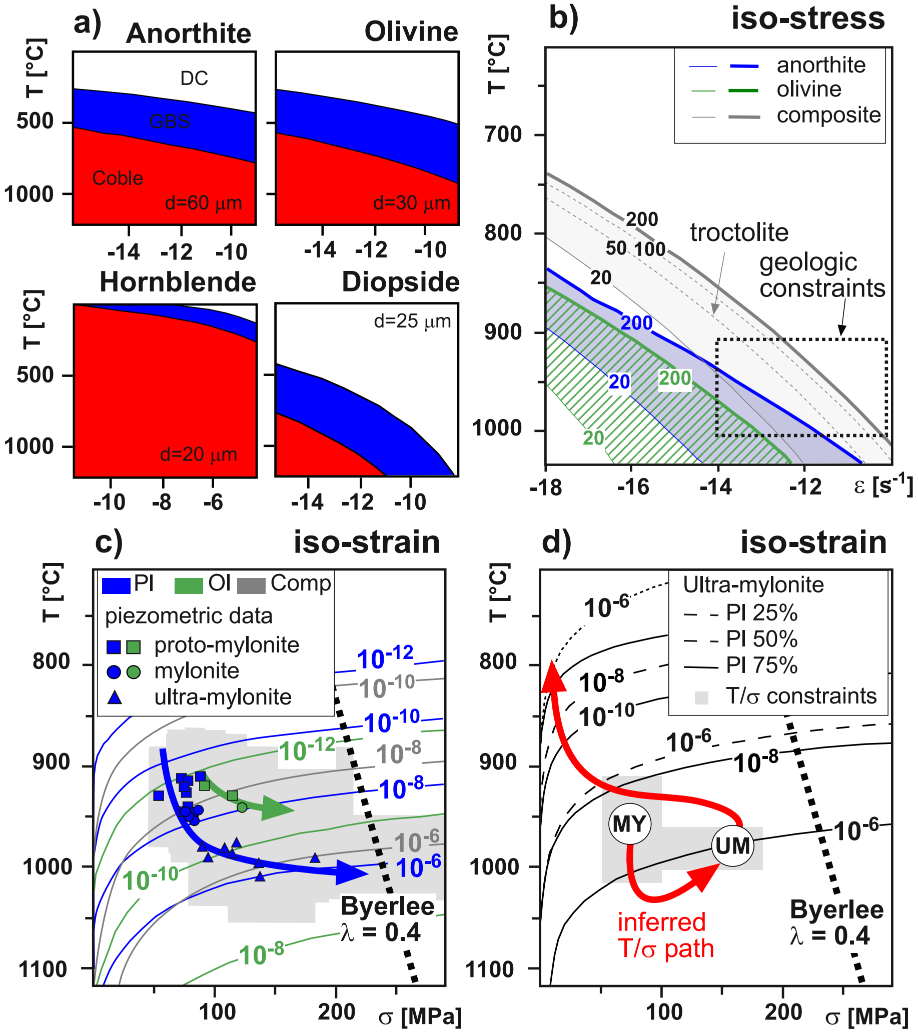

**Figure 8.** Rheological models: (a) deformation mechanism maps in *T*/strain-rate space of dry anorthite (taken as representative of plagioclase), diopside (taken as representative of clino/orthopyroxene behavior), hornblende (taken as representative of amphibole), and dry olivine; (b) strength profiles calculated for anorthite (blue), olivine (green), and composite troctolite assuming an iso-stress mechanical boundary condition. The profiles are drawn in T/strain-rate space for various stress values; stress is expressed in MPa; (c) strength profiles calculated for anorthite (blue), olivine (green) and composite troctolite assuming an iso-strain rate mechanical boundary condition. The profiles are drawn in *T*/stress space for various strain-rates. The stress values calculated from plagioclase and olivine grain size are also shown for comparison. The gray shaded area represents *T*-stress constraints calculated by combining the available thermometry and piezometric couples; (d) strength profiles calculated for a bimineralic plagioclase + amphibole mixture with variable composition, assuming an iso-strain rate mechanical boundary condition. The gray-shaded area represents the mean *T*-stress conditions inferred for the development of mylonite (MY) and ultra-mylonite (UM) fabric. The red arrows denote the inferred deformational path.

(Hobbs et al., 2019; Soda et al., 2019). Finally, amphibole CPO's are consistent with a joint activity on [001] (100) and [001] (010) slip systems, and show a progressive increase of fabric intensity in the ultra-mylonite with respect to other domains; that is the amphibole CPO trend is opposite to that of plagioclase.

### 5.2. Deformation Mechanisms in the Proto-Mylonite and Mylonite

The temperature of equilibration for the plagioclase-amphibole pairs measured in the slightly deformed troctolites is ~1040°C (Sanfilippo et al., 2019), which is nearly coincident with the solidus temperature of magmatic amphibole. Here, the large Ti-pargasite oikocrysts preserve magmatic textures with irregular grain boundaries terminating in film-like apophyses, and locally include corroded Plagioclase grains. However, some of these Ti-pargasite-plagioclase microdomains are deformed, thereby indicating that high-temperature shearing followed complete crystallization of the rock.

The microstructure and plagioclase CPO patterns for proto-mylonite and mylonite are overall suggestive of grain-size reduction by dislocation creep (Handy et al., 1999; Mehl & Hirth, 2008; Stipp & Tullis, 2003). The size of the subgrains within the porphyroclasts is similar to that of the recrystallized grains in the surrounding matrix, indicating that grain-size reduction involved cooperative sub-grain rotation and grain-boundary migration (Stipp & Tullis, 2003). This interpretation is further confirmed by the high frequency of low angles <5°–10° detected by misorientation-angle distribution, which indicates either inheritance of subgrain boundaries from the porphyroclasts, or dislocation creep being active in the matrix (Svahnberg & Piazolo, 2010). All these observations indicate that deformation promoting grain-size reduction occurred under sub-solidus conditions. However, the mylonite matrix displays occasional four-grain junctions, fracturing of porphyroclasts and rotation of rigid fragments (Figures 5a–5d), combined with a decrease in plagioclase CPO (Figure 7b), as typically observed in granular frictional-viscous mylonite (Handy et al., 1999; Menegon et al., 2013). Furthermore, a local presence of small fractions of syn-deformational melt is evidenced by the texture of the Ti-pargasite within the mylonite (Figures 3a and 3b).

The slight decrease of plagioclase CPO could derive from destruction of an inherited magmatic fabric by incipient dislocation creep on [100] (010) or [100] (001) slip systems. However, this hypothesis can be rejected as the strain gradient marking the transition from mylonite to ultra-mylonite indicates protracted deformation, which would have increased the fabric intensity. Alternatively, the combination of incipient microstructure typical of granular flow in presence of thin melt films (Figures 3a, 3b, and 5a–5d), a weak plagioclase CPO (Figure 7b), and the minor intensity of crystal-plastic deformation in the weaker mylonitic layers of recrystallized grains, may suggest a switch from grain-size insensitive dislocation creep to diffusion creep (Handy et al., 1999; Hobbs et al., 2019; Platt, 2015).

### 5.3. Deformation Mechanisms in the Ultra-Mylonite

The ultra-mylonite domain has distinctive mineralogical and chemical characteristics, coupled with different microstructure and texture, compared to the host mylonite. The plagioclase CPO in the ultra-mylonite, though still consistent, is slightly weaker than in the mylonite. The other major constituent of the ultra-mylonite, amphibole, shows both a stronger CPO and more pronounced SPO, with most crystals elongated at 38° to the stretching direction. The development of CPO and shape preferred orientation in highly deformed shear zones is generally interpreted as evidence of dislocation creep (Gomez-Barreiro et al., 2007; Mehl & Hirth, 2008). Yet, exceptions are reported from experiments conducted in the low-stress regime, which show that strong textures and preferred mineral orientations may also develop in the Newtonian regime during diffusion creep (e.g., Gomez-Barreiro et al., 2007), or cooperative diffusion creep and grain-boundary sliding (Soda et al., 2019). Although conclusive microstructural evidences for GBS are rarely reported, we postulate that the ultra-mylonite reflects a switch from dominant dislocation creep to diffusion-accommodated Lifschitz grain-boundary sliding (Bestmann & Prior, 2003; Dimanov et al., 2007; Drury & Humphreys, 1988; Jiang et al., 2000). One main argument supporting the activation of GBS is the extremely fine grain size of the plagioclase + Ti-pargasite aggregate (Figure 8b and Table 1), which is far below the minimum equilibrium grain size required for dislocation creep (>40–50 μm; De Bresser et al., 2001; Rybacki & Dresen, 2000). Moreover, dislocation creep alone cannot explain the extensive phase mixing, or the compositional change observed in the ultra-mylonite relative to the other domains (Figure 8a). The proposed mechanism is also consistent with the slight decrease of plagioclase CPO intensity (Figure 7). In fact, sustained dislocation creep would have produced a net increase of fabric intensity relative to mylonite, as the degree of CPO development is roughly proportional to finite strain. Thus, it is unlikely that dislocation creep was the dominant deformation mechanism in the ultra-mylonite. In addition, weak CPO may also otherwise develop in response to superplastic flow by preferential diffusion along stress gradients, a process required to maintain the mechanical compatibility during rotation and displacement of grains (Dimanov et al., 2007; Hobbs et al., 2019; Papa et al., 2020). Microstructural observations further confirm this interpretation. For instance, neoblastic grains in the ultra-mylonite are almost devoid of structures suggestive of internal strain. Besides, subgrain boundaries are rare, and the misorientation angles decrease, although some degree of misorientation still occurs along the grain boundaries. Plagioclase grains are mostly isolated within very fine-grained aggregates of Ti-pargasite, which show abundant structure typical of granular flow (Figures 3e, and 5e–5g). These observations are fully consistent with superplastic flow activated by grain-size sensitive diffusion process (Hobbs et al., 2019; Menegon et al., 2013, 2015; Papa et al., 2020).

Superplastic flow requires low cohesion of the grain boundaries (Drury & Humphreys, 1988; Précigout et al., 2007; Zhao et al., 2019). This easy-glide condition is typically enhanced by high dislocation densities, metamorphic fluids, or by networks of weak minerals (Handy et al., 1999). The magmatic composition of the Ti-pargasite formed during the high-temperature deformation event recorded here (T close to 1000°C), and the essentially anhydrous composition of the host troctolite, suggest that seawater-derived fluids were absent during strain localization. Yet, sufficient microstructural lubrication could have been provided by the widespread occurrence of Ti-pargasite, which enhanced strain by easy slip along the (010) planes, thereby facilitating the rotation of plagioclase grains (Gomez-Barreiro et al., 2007; Langdon, 2006; Soda et al., 2019). A similar mechanism has been proposed for low-grade metamorphic rocks and clay-rich sediments (Casini & Funedda, 2014; Schuck et al., 2020), yet the potential softening related to accumulation of Ti-pargasite becomes obvious at $T > 800°C$ in an amphibole-rich ultra-mylonite (Figure 8d). We must consider, however, that the equilibration temperature of the plagioclase-amphibole pairs in the ultra-mylonite (~900°C–1000°C) is very close to the solidus of the Ti-rich pargasite (<1000°C, e.g., Koepke et al., 2004, 2018). Thus, rather than lubricated by solid amphibole, it is possible that the strain localization was assisted by the presence of a melt phase. The occurrence of melt is required to explain the bulk chemical composition of the ultra-mylonite, which is markedly enriched in water, titanium, alkalis, and other in incompatible elements compared to the host mylonitic troctolite. In addition, melt-present deformation would explain the absence of a well-equilibrated texture in the ultra-mylonite. The localization of late Fe-Ti rich melts in crystal-plastically deformed shear zones, for example, is ubiquitous in the Atlantis Bank gabbro batholith on the SW Indian Ridge. Thus, this would hardly be a unique occurrence. The circulation of interstitial melt by the instauration of a dynamic porosity (Fusseis et al., 2009; Papa et al., 2020) might have further contributed to decrease the shear resistance of the composite acting as a critical factor for stabilizing diffusion creep and GBS in the core of the shear zone.

### 5.4. Stress and Strain-Rate Evolution

The bulk strength of a compositionally heterogeneous mylonite is expected to change so long as the grain size and the topology of its constituent phases changes in response to dynamic recrystallization. At a steady state, however, the microstructure is in equilibrium with the flow stress and the strain rate stabilizes around a critical value (Appendix B). Theoretical arguments suggest that shear zones evolve at approximately constant stress as long as the mechanical boundary conditions remains unchanged, and the shear zone is sufficiently homogeneous (Platt & Behr, 2011). The OCC sampled at 16.5°N on the Mid Atlantic Ridge largely matches these requirements, as: (a) detachment faults reflect quite simple stress fields persisting over several millions of years, and (b) the composition of troctolite is remarkably homogeneous at a scale of tens to hundreds of meters, typical of oceanic shear zones (Hansen et al., 2013).

Thus, the mylonite/ultra-mylonite transition likely reflects an abrupt increase of strain rate and localization in response to dramatic weakening, as already proposed in felsic rocks showing equivalent microstructural evolution (Casini & Funedda, 2014; Menegon et al., 2013). This hypothesis might be scrutinized in relation to the differential stress captured by the shear zones different microstructural domains. We must emphasize that any assumption about the magnitude of differential stress in the ultra-mylonite zone is speculative, as piezometric relations based on recrystallized grain-size are calibrated for monophase rocks deforming by dislocation creep (Twiss, 1977). Yet, the sequence of microstructure development, the monotonic decrease of grain size, and the increase of phase mixing from proto-mylonite to ultra-mylonite, all indicate that dislocation creep predates activation of any grain-size sensitive processes. Thus, because neither diffusion-facilitated GBS nor diffusion creep would have promoted grain-size reduction in the ultra-mylonite, we can speculate that plagioclase grains record approximately the maximum differential stress prior to switching to superplasticity (De Bresser et al., 2001). Based on this assumption, the mylonite/ultra-mylonite transition might corresponds to a local increase of both strain rate, from $1 \times 10^{-9}$ to $5 \times 10^{-7}\ s^{-1}$, and differential stress, from about 60 to 200 MPa (Figure 8c). If this interpretation is correct, the development of ultra-mylonite reflects strain weakening driven by a switch from dislocation creep to a grain-size sensitive mechanism and occurred at high strain rate, possibly approaching sub-seismic velocity.

### 5.5. High-Temperature Strain Localization

Our data suggest that the deformed troctolites from the Mid Atlantic Ridge16.5°N OCC record a switch from grain-size insensitive dislocation creep to diffusion creep, associated with diffusion accommodated Lifschitz GBS. Theoretical deformation behavior derived from empirical flow laws are in good agreement with the microstructures, CPO and shape preferred orientation patterns of the mylonitic and ultra-mylonitic domains. GBS has been occasionally proposed as fundamental mechanism to induce strain localization in the lithosphere, and can be ultimately related to the nucleation of an oceanic detachment (i.e., Mehl & Hirth, 2008; Miranda et al., 2016; Précigout et al., 2007; Svahnberg & Piazolo, 2010). This mechanism is activated by fine-grain size and high differential stress, which allow particle flow. The relative displacements between adjacent grains produced by GBS, combined with grain boundary diffusion, result in phase mixing. This in turn inhibits grain growth because of Zenner pinning further promoting localization in the ductile regime (Mehl & Hirth, 2008; Précigout et al., 2007; Soda et al., 2019). However, strain localization in the oceanic crust is generally expected during cooling (MacLeod et al., 2017; Miranda & John, 2010), as sustained by the common occurrence of ultra-mylonite bands developed at amphibole facies conditions in other OCC's (e.g., Miranda & John, 2010; MacLeod et al., 2017; Basch et al., 2020).

The case reported here reveals that the synchronous development of diffusion creep and GBS mechanisms requires an increase of temperature from the proto-mylonite toward the ultra-mylonite (Figure 1). As such, the shear zone provides a unique case of strain localization at high temperatures. The different mineralogical and geochemical compositions of the ultra-mylonite compared to the host troctolite precludes the possibility that the transition to GBS was driven by a metamorphic reaction between a former mylonite and seawater-derived fluids, which could not account for the enrichment in titanium. Indeed, the extremely high temperature of equilibration and the abundance of Ti-pargasitic amphibole require the occurrence of a magmatic component rich in water, silica and immobile elements such as Ti. Two competing hypotheses can be proposed to explain the occurrence of melt in the ultra-mylonite: (a) localization of melt already present in the troctolite, or (b) remelting of troctolite amphibole-rich domains. The first hypothesis implies syn-tectonic hybridization from a melt rich in $H_2O$ and incompatible elements. These late-stage melts are not rare in the oceanic lithosphere, where they crystallize felsic lithologies characterized by amphibole and albitic plagioclase intruded within more primitive gabbros (Basch et al., 2020; Dick et al., 2019; Ma et al., 2020; MacLeod et al., 2017). For instance, Gardner et al. (2020) recently showed that the injection of these late-stage melts within a deforming olivine-gabbro in the Atlantis Bank promoted strain localization necessary for nucleation of the oceanic detachment. The origin of melts forming felsic lithologies is debated and include extreme fractional crystallization starting from a basaltic melt (e.g., Nguyen et al., 2018; Basch et al., 2020) or partial melting of preexisting hydrothermally altered gabbros (France et al., 2013; Koepke et al., 2007), or both (Ma et al., 2020). The anomalous composition of the ultra-mylonite could be thus interpreted as resulting from hybridization of a felsic melt localized in the shear zone by crystal plastic deformation. However, felsic lithologies are always characterized by albitic plagioclase (An <40 mol%), and commonly contain late-stage phases such as zircons and apatite (see MacLeod et al., 2017 for a review). Yet, the clear deformation gradient highlighted by the transition from proto-mylonite to mylonite and ultra-mylonite (Figure 1b) is not correlated with the compositional gradient expected during a process of chemical hybridization. This observation, together with the preservation of high An in plagioclase (65 mol.%), the high modal abundance of Ti-pargasite, the lack of zircon and apatite as accessory phases and the absence of felsic veins elsewhere in the dredge hauls (see Sanfilippo et al., 2019) make this hypothesis unlikely.

On the other hand, the second hypothesis implies that the "hybrid" nature of this melt derives from selective re-melting of interstitial amphibole-plagioclase micro-domains, which we observe randomly distributed in the weakly deformed troctolites in the same dredge hauls (Figure 2b). Microstructural evidence shows that troctolite was completely solidified at the onset of deformation, although the temperature at which the deformation event took place were close to the solidus temperature of the interstitial Ti-pargasite (Figure 2b). The mylonite and ultra-mylonite preserve localized textural evidences for small fraction of syn-deformation melt within the neoblastic matrix, which support this interpretation (Figure 3). Although the heat source necessary for re-melting is unknown, our observations at the 16.5°N OCC might strengthen the existing connection between deformation and heating (Burg & Gerya, 2005; Maino et al., 2015, 2020). However, we cannot assume a priori that shear heating might have overcome the conductive heat loss, yielding to the development of a stable shear zone. Further investigations are required to propose a comprehensive explanation of this process.

## 6. Conclusions

Microstructural analyses were performed on variably deformed troctolites from the Mid Atlantic Ridge 16.5°N OCC. Selected samples show a marked deformation gradient developed in a decimeter-scale shear zone. Deformation is estimated to have progressed at increasing temperature from ∼900°C to ∼1100°C from the proto-mylonite toward the mylonite-ultra-mylonite boundary.

The proto-mylonite and mylonite show core and mantle plagioclase porphyroclasts, subgrains and strain-free recrystallized new grains suggesting that strain is mainly accommodated by combined subgrain-rotation and grain boundary migration. However, narrow, fine-grained recrystallized layers preserve microstructures and CPO patterns suggestive of incipient diffusion creep. This latter mechanism become dominant in the ultra-mylonite band, as testified by a dramatic reduction of grain size (<10 μm), substantial increase of the phase mixing, associated with weakening of the plagioclase CPO but enhanced shape preferred orientation and CPO intensity of amphibole. Paleopiezometry and rheological modeling reveal that these microstructural changes correspond to the transition from power-law creep to Newtonian creep and grain boundary sliding. Therefore, we propose that the deformation mechanism switch has resulted into a dramatic decrease of strength in the ultra-mylonite, providing the necessary softening for shear localization at high temperature conditions close to the solidus of troctolite. Weakening was promoted by the presence of amphibole and melt, which acted as microstructural lubricant that facilitated grain boundary sliding localizing deformation in a narrow shear zone.

The melt present during the development of the ultra-mylonite studied here was either (a) a felsic melt produced by differentiation in a crystal mush, and successively injected into the deforming assemblage or (b) the product of selective melting of intergranular domains (amphibole + plagioclase) triggered by deformation at high temperature conditions. Geochemical signature of the ultra-mylonite hints for the second origin, suggesting that the presence and distribution of hydrous magmatic phases may be a critical factor for localizing deformation in OCC, finally promoting the nucleation of detachment faults.

## Appendix A: Phase Mixing

The intensity of phase mixing is assumed to be roughly proportional to the cumulative length of phase boundaries per unit surface and is computed from EBSD maps as:

$$\boldsymbol{\mu} = \frac{\sum_{i=1}^{N} \boldsymbol{L_i}}{\boldsymbol{A}} \boldsymbol{k} \tag{A1}$$

where $\mu$ represents the degree of phase mixing (mm$^{-1}$), $L_i$ (mm) is phase boundary density corresponding to cumulative length of phase boundary in a domain of area A (mm$^2$) containing $i$ phases (Cross & Skemer, 2017). $K$ is a normalization factor computed as $K = (8r\pi)^2$ that represents the maximum value of phase boundary density assuming perfectly circular grains of radius $r$. Given a minimum grain diameter of 3 μm, which is consistent with the spatial resolution of EBSD phase mapping, theoretical phase mixing intensities range from 0 to 1.

## Appendix B: Rheological Modelling

The relationships among deformation mechanisms, grain size, stress, and strain-rate at various temperature conditions have been investigated by calculating stress- and strain rate-temperature profiles for a composite made of olivine + anorthite + pyroxene + amphibole in modal proportion matching that of troctolite. We assume that the composite is homogeneous and each phase have a characteristic grain size coincident with the median grain size calculated from EBSD analysis (Table 1). The deformation mechanisms considered in our simplified model are dislocation creep, Coble creep and Lifschitz diffusion-accommodated grain-boundary sliding (Langdon, 2006; Lifshitz, 1963). Taken individually, the viscous creep of each phase within the composite material follows a similar Arrhenius-type equation:

$$\dot{\varepsilon}_i = A_i \sigma_i^{n_i} d_i^{-p_i} \exp\left(-\frac{Q_i}{RT}\right) \quad \text{(A2)}$$

where $A_i$ is a pre-exponential constant (MPa$^{-n}$μm$^{p}$s$^{-1}$), $n_i$ is the stress exponent, $d_i$ is the grain size (μm), $p_i$ is the grain size exponent, $Q_i$ is the activation energy (kJmol$^{-1}$), $T$ is temperature (K) and $R$ is the gas constant. The constitutive parameters $A$, $n$, $p$, and $Q$ in Equation A2 have different values depending on the active deformation mechanism (Supporting Information S1, Table S1). The flow law of composite troctolite is derived assuming that different deformation mechanisms cooperate in parallel but are internally competitive within each phase, so that the bulk infinitesimal strain-rate $\dot{\varepsilon}_b$ of the composite is:

$$\dot{\varepsilon}_b = \sum_j \dot{\varepsilon}_j \phi_j \quad \text{(A3)}$$

where the term $\phi_j$ represents the molar volumetric proportion of the $j$th phase calculated from the volume proportions $V_j$ and molar volumes $V_j^m$ as (Hobbs et al., 2019):

$$\phi_j = \frac{\prod_j V_j V_j^m}{\sum_j V_j a_j} \quad \text{(A4)}$$

$$a_j = \sum_{j \neq i} V_i^m \quad \text{(A5)}$$

The constitutive equation of the composite is then obtained by substituting Equation A2 into A3:

$$\dot{\varepsilon}_b = A\sigma^n D \exp\left(-\frac{Q}{RT}\right) \quad \text{(A6)}$$

The constitutive parameters of the composite (Equations A7–A14) are then calculated assuming that either strain rate or stress is uniform within the composite (Handy et al., 1999; Hobbs et al., 2019; Huet et al., 2014; Reuss, 1929; Voigt, 1928). Using the first of these two mechanical constraints (iso-strain rate condition) implies that stress might be nonuniform; thus, the effective deformation mechanism operating in each phase is the one that minimizes local stress $\sigma_j$ and the parameters of Equation A6 are calculated according to (Hobbs et al., 2019):

$$n = \frac{\prod_j n_j}{\sum_j b_j \phi_j} \quad \text{(A7)}$$

$$A = \prod_j A_j^{\phi_j n / n_j} \quad \text{(A8)}$$

$$Q = n \sum_j \frac{\phi_j Q_j}{n_j} \quad \text{(A9)}$$

$$D = \prod_j d_j^{-\frac{p_j n}{n_j}} \quad \text{(A10)}$$

where the term $b_j$ in Equation A7 represents the product of all phase stress exponents excluding that of the $j$th phase. On the other hand, using the iso-stress condition the effective deformation mechanism is the one that maximizes the local strain rate $\dot{\varepsilon}_j$ as (Equations A11–A14):

$$n = \sum_j \phi_j n_j \quad \text{(A11)}$$

$$A = \prod_j A_j^{\phi_j} \quad \text{(A12)}$$

$$\boldsymbol{Q} = \sum\nolimits_j \phi_j \boldsymbol{Q}_j \tag{A13}$$

$$\boldsymbol{D} = \prod\nolimits_j \boldsymbol{d}_j^{-\frac{\phi_j}{p_j}} \tag{A14}$$

The strength profiles for pure anorthite, diopside, and olivine have been calculated with the parameters given by Rybacki and Dresen (2000), Dimanov et al. (2007), and Hirth and Kohlstedt (2003), respectively, and used for comparison in stress and strain rate-temperature plots (Figure 8).

## Data Availability Statement

The data set used in this study will be stored into Mendely data repository http://dx.doi.org/10.17632/3kthrpngct.1.

**Acknowledgments**
The authors wish to thank Christophe Nevado and Doriane Delmas for careful thin section preparation and Fabrice Barou for helpful assistance during EBSD measurements. We thank the captain and crew of the R/V Knorr for their help and enthusiasm during our cruise to the 16.5° core complexes. Fuwu Ji, Joe Cann, Deborah Smith, Hans Schouten, and Ross Parnell-Turner assisted in dredging, sample description, and provide the authors with considerable insight into the geologic and geophysical data collected during the Knorr cruise 210 Leg 5. L. Casini thanks to Regione Autonoma della Sardegna for partly supporting this research (RASSR14473), and Università degli studi di Sassari (FAR2019). Funding for H. Dick was provided by US National Science Foundation grant No. 1935837. Open access funding enabled and organized by Projekt DEAL.

## References

Allard, M, Ildefonse, B., & Olliot, E. (2020). Plastic deformation of plagioclase in a gabbro pluton at a slow-spreading ridge (IODP Hole U1473A, Atlantis Bank, Southwest Indian ridge). In *AGU fall meeting 2020*. https://doi.org/10.5194/egusphere-egu21-4089

Basch, V., Sanfilippo, A., Sani, C., Ohara, Y., Snow, J., Ishizuka, O., et al. (2020). Crustal accretion in a slow spreading back-arc basin: Insights from the MadoMegamullion oceanic core complex in the Shikoku Basin. *Geochemistry, Geophysics, Geosystems*, *21*(11), e2020GC009199. https://doi.org/10.1029/2020gc009199

Bercovici, D., & Karato, S. I. (2002). Theoretical analysis of shear localization in the lithosphere. *Reviews in Mineralogy and Geochemistry*, *51*, 387–420. https://doi.org/10.2138/gsrmg.51.1.387

Bestmann, M., & Prior, D. J. (2003). Intragranular dynamic recrystallization in naturally deformed calcite marble: Diffusion accommodated grain boundary sliding as a result of subgrain rotation recrystallization. *Journal of Structural Geology*, *25*(10), 1597–1613. https://doi.org/10.1016/s0191-8141(03)00006-3

Burg, J. P., & Gerya, T. V. (2005). The role of viscous heating in Barrovian metamorphism of collisional orogens: Thermomechanical models and application to the Lepontine Dome in the Central Alps. *Journal of Metamorphic Geology*, *23*, 75–95. https://doi.org/10.1111/j.1525-1314.2005.00563.x

Casini, L., & Funedda, A. (2014). Potential of pressure solution for strain localization in the BaccuLocci Shear Zone (Sardinia, Italy). *Journal of Structural Geology*, *66*, 188–204. https://doi.org/10.1016/j.jsg.2014.05.016

Cross, A. J., & Skemer, P. (2017). Ultra-mylonite generation via phase mixing in high-strain experiments. *Journal of Geophysical Research: Solid Earth*, *122*, 1744–1759. https://doi.org/10.1002/2016JB013801

De Bresser, J. H. P., TerHeege, J. H., Spiers, C. J., TerHeege, J. H., & Spiers, C. J. (2001). Grain size reduction by dynamic recrystallization: Can it result in major rheological weakening? *International Journal of Earth Sciences*, *90*, 28–45. https://doi.org/10.1007/s005310000149

Dick, H. J. B., Mac Leod, C. J., Plum, P., Abe, N., Blackman, D. K., Bowles, J. A., et al. (2019). Dynamic accretion beneath a slow-spreading ridge segment: IODP Hole 1473A and the Atlantis Bank oceanic core complex. *Journal of Geophysical Research, Solid Earth*, *124*, 12631–12659. https://doi.org/10.1029/2018JB016858

Dick, H. J. B., Natland, J. H., Alt, J. C., Bach, W., Bideau, D., Gee, J. S., et al. (2000). A long in situ section of the lower ocean crust: Results of ODP Leg 176 drilling at the Southwest Indian Ridge. *Earth Planet. Sci. Lett.*, *179*, 31–51. https://doi.org/10.1016/S0012-821X(00)00102-3

Drury, M. R., & Humphreys, F. J. (1988). Microstructural shear criteria associated with grain-boundary sliding during ductile deformation. *Journal of Structural Geology*, *10*(1), 83–89. https://doi.org/10.1016/0191-8141(88)90130-7

Escartín, J., Smith, D. K., Cann, J., Schouten, H., Langmuir, C. H., & Escrig, S. (2008). Central role of detachment faults in accretion of slow-spreading oceanic lithosphere. *Nature*, *455*(7214), 790–794. https://doi.org/10.1038/nature07333

France, L., Ildefonse, B., & Koepke, J. (2013). Hydrous magmatism triggered by assimilation of hydrothermally altered rocks in fossil oceanic crust (northern Oman ophiolite). *Geochemistry, Geophysics, Geosystems*, *14*(8), 2598–2614. https://doi.org/10.1002/ggge.20137

Fusseis, F., Regenauer-Lieb, K., Liu, J., Hough, R. M., & De Carlo, F. (2009). Creep cavitation can establish a dynamic granular fluid pump in ductile shear zones. *Nature*, *459*, 974–977. https://doi.org/10.1038/nature08051

Gardner, R. L., Piazolo, S., Daczko, N. R., & Trimby, P. (2020). Microstructures reveal multistage melt present strain localisation in mid-ocean gabbros. *Lithos*, *366-367*, 105572. https://doi.org/10.1016/j.lithos.2020.105572

Gomez-Barreiro, J., Lonardelli, I., Wenk, H. R., Dresen, G., Rybacki, E., Ren, Y., & Tomé, C. N. (2007). Preferred orientation of anorthite deformed experimentally in Newtonian creep. *Earth and Planetary Science Letters*, *264*, 188–207. https://doi.org/10.1016/j.epsl.2007.09.018

Handy, M.R., Wissing, S.B., & Streit, L.E. (1999). Frictional-viscous flow in mylonite with varied bimineralic composition and its effect on lithospheric strength. *Tectonophysics*, *303*, 175–191. https://doi.org/10.1016/s0040-1951(98)00251-0

Hansen, L. N., Cheadle, M. J., John, B. E., Swapp, S. M., Dick, H. J. B., Tucholke, B. E., & Tivey, M. A. (2013). Mylonitic deformation at the Kane oceanic core complex: Implications for the rheological behavior of oceanic detachment faults. *Geochemistry, Geophysics, Geosystems*, *14*, 3085–3108. https://doi.org/10.1002/ggge.20184

Hobbs, B. E., Ord, A., Ulrich, S., & Schulmann, K. (2019). Rheology of mixed deformation mechanisms and mineral phase assemblages. *Journal of Structural Geology*, *129*, 103891. https://doi.org/10.1016/j.jsg.2019.103891

Holland, T., & Blundy, J. (1994). Non-ideal interactions in calcic amphiboles and their bearing on amphibole-plagioclase thermometry. *Contributions to mineralogy and petrology*, *116*(4), 433–447. https://doi.org/10.1007/bf00310910

Huet, B., Yamato, P., & Grasemann, B. (2014). The minimized power geometric model: An analytical mixing model for calculating polyphase rock viscosities consistent with experimental data. *Journal of Geophysical Research*, *119*, 3897–3924. https://doi.org/10.1002/2013jb010453

Ildefonse, B., Blackman, D. K., John, B. E., Ohara, Y., Miller, D. J., & MacLeod, C. J. (2007). Oceanic core complexes and crustal accretion at slow-spreading ridges. *Geology*, *35*(7), 623–626. https://doi.org/10.1130/g23531a.1

Jiang, Z., Prior, D. J., & Wheeler, J. (2000). Albite crystallographic pre ferred orientation and grain misorientation distribution in a low grade mylonite: Implications for granular flow. *Journal of Structural Geology*, *22*, 1663–1674. https://doi.org/10.1016/s0191-8141(00)00079-1

Jöns, N., Bach, W., & Schroeder, T. (2009). Formation and alteration of plagiogranites in an ultramafic-hosted detachment fault at the Mid Atlantic Ridge (ODP Leg 209). *Contribution tu mineralogy and Petrology*, *157*, 625–639. https://doi.org/10.1007/s00410-008-0357-2

Koepke, J., Berndt, J., Feig, S. T., & Holtz, F. (2007). The formation of $SiO_2$-rich melts within the deep oceanic crust by hydrous partial melting of gabbros. *Contributions to Mineralogy and Petrology*, *153*(1), 67–84. https://doi.org/10.1007/s00410-006-0135-y

Koepke, J., Botcharnikov, R. E., & Natland, J. H. (2018). Crystallization of late-stage MORB under varying water activities and redox conditions: Implications for the formation of highly evolved lavas and oxide gabbro in the ocean crust. *Lithos*, *323*, 58–77. https://doi.org/10.1016/j.lithos.2018.10.001

Koepke, J., Feig, S. T., Snow, J., & Freise, M. (2004). Petrogenesis of oceanic plagiogranites by partial melting of gabbros: An experimental study. *Contributions to Mineralogy and Petrology*, *146*(4), 414–432. https://doi.org/10.1007/s00410-003-0511-9

Langdon, T.G (2006). Grain boundary sliding revisited: Developments in sliding over four decades. *J. Mater. Sci.*, *41*, 597–609. https://doi.org/10.1007/s10853-006-6476-0

Lifshitz, I. M. (1963). On the theory of diffusion-viscous flow of polycrystalline bodies. *Soviet Physics JETP*, *17*(4), 909.

Ma, Q., Dick, H. J., Urann, B., & Zhou, H. (2020). Silica-rich vein formation in an evolving stress field, Atlantis Bank Oceanic core complex. *Geochemistry, Geophysics, Geosystems*, *21*(7), e2019GC008795. https://doi.org/10.1029/2019gc008795

MacLeod, C. J., Dick, H. J. B., Blum, P., Abe, N., Blackman, D. K., Bowles, J. A., et al. (2017). *Hole 1105A redescription* (p. 360). the Expedition.

Maino, M., Casini, L., Boschi, C., Setti, M., Di Giulio, A., & Seno, S. (2020). Time-dependent heat budget of a thrust from geological records and numerical experiments. *Journal of Geophysical Research, Solid Earth*, *125*. https://doi.org/10.1029/2019JB018940

Maino, M., Casini, L., Ceriani, A., Decarlis, A., Di Giulio, A., Seno, S., et al. (2015). Dating shallow thrusts with zircon (U-Th)/He thermochronometry: The shear heating connection. *Geology*, *43*(6), 495–498. https://doi.org/10.1130/g36492.1

Mehl, L., & Hirth, G. (2008). Plagioclase preferred orientation in layered mylonites: Evaluation of flow laws for the lower crust. *Journal of Geophysical Research*, *113*, B05202. https://doi.org/10.1029/2007JB005075

Menegon, L., Fusseis, F., Stünitz, H., & Xiao, X. (2015). Creep cavitation bands control porosity and fluid flow in lower crustal shear zones. *Geology*, *43*(3), 227–230. https://doi.org/10.1130/g36307.1

Menegon, L., Stünitz, H., Nasipuri, P., Heilbronner, R., & Svahnberg, H. (2013). Transition from fracturing to viscous flow in granulite faciesperthitic feldspar (Lofoten, Norway). *Journal of Structural Geology*, *48*, 95–112. https://doi.org/10.1016/j.jsg.2012.12.004

Miranda, E.A., Hirth, G., & John, B.E. (2016). Microstructural evidence for the transition from dislocation creep to dislocation-accommodated grain boundary sliding in naturally deformed plagioclase. *Journal of Structural Geology*, *92*, 30–45. https://doi.org/10.1016/j.jsg.2016.09.002

Miranda, E. A., & John, B. E. (2010). Strain localization along the Atlantis Bank oceanic detachment fault system, Southwest Indian Ridge. *Geochemistry, Geophysics, Geosystems*, *11*(4). https://doi.org/10.1029/2009gc002646

Nguyen, D. K., Morishita, T., Soda, Y., Tamura, A., Ghosh, B., Harigane, Y., et al. (2018). Occurrence of felsic rocks in oceanic gabbros from IODP hole U1473A: Implications for evolved melt migration in the lower oceanic crust. *Minerals*, *8*(12), 583. https://doi.org/10.3390/min8120583

Parnell-Turner, R., Schouten, H., & Smith, D. K. (2016). Tectonic structure of the Mid-Atlantic Ridge near 16° 30′ N. *Geochemistry, Geophysics, Geosystems*, *17*(10), 3993–4010. https://doi.org/10.1002/2016gc006514

Platt, J. P. (2015). Rheology of two-phase systems: A microphysical and observational approach. *Journal of Structural Geology*, *77*, 213–227. https://doi.org/10.1016/j.jsg.2015.05.003

Platt, J. P., & Behr, W. M. (2011). Lithospheric shear zones as constant stress experiments. *Geology*, *33*, 537–130. https://doi.org/10.1130/G31561.1

Précigout, J., Gueydan, F., Gapais, D., Garrido, C. J., & Essaifi, A. (2007). Strain localisation in the subcontinental mantle: A ductile alternative to the brittle mantle. *Tectonophysics*, *445*, 318–336. https://doi.org/10.1016/j.tecto.2007.09.002

Reuss, A. (1929). Berechnung der Fliessgrenze von Mischkristallen auf Grund der Plastizitätsbedingung für Einkristalle. *ZAMM-Zeitschrift für Angewandte Mathematik und Mechanik*, *9*, 49–58. https://doi.org/10.1002/zamm.19290090104

Rutter, E. H. (1997). The influence of deformation on the extraction of crustal melts: A consideration of the role of melt-assisted granular flow. *Mineralogical society series*, *8*, 82–110.

Rybacki, E., & Dresen, G. (2000). Dislocation and diffusion creep of synthetic anorthite aggregates. *Journal of Geophysical Research*, *105*, 26017–26036. https://doi.org/10.1029/2000jb900223

Sanfilippo, A., Dick, H. J. B., Marschall, H. R., Lissenberg, C. J., & Urann, B. (2019). Emplacement and high-temperature evolution of gabbros of the 16.5°N oceanic core complexes (Mid-Atlantic Ridge): Insights into the compositional variability of the lower oceanic crust. *Geochemistry, Geophysics, Geosystems*, *20*, 46–66. https://doi.org/10.1029/2018GC007512

Satsukawa, T., Ildefonse, B., Mainprice, D., Morales, L. F. G., Michibayashi, K., & Barou, F. (2013). A database of plagioclase crystal preferred orientations (CPO) and microstructures–implications for CPO origin, strength, symmetry and seismic anisotropy in gabbroic rocks. *Solid Earth*, *4*, 511–542. https://doi.org/10.5194/se-4-511-2013

Schuck, B., Desbois, G., & Urai, J. L. (2020). Grain-scale deformation mechanisms and evolution of porosity in experimentally deformed Boom Clay. *Journal of Structural Geology*, *130*, 103894. https://doi.org/10.1016/j.jsg.2019.103894

Smith, D. K., Escartin, J., Cannat, M., Tolstoy, M., Fox, C. G., Bohnenstiehl, D. R., & Bazin, S. (2003). Spatial and temporal distribution of seismicity along the northern Mid-Atlantic Ridge (15°–35° N). *Journal of Geophysical Research*, *108*(B3). https://doi.org/10.1029/2002jb001964

Smith, D. K., Schouten, H., Dick, H. J., Cann, J. R., Salters, V., Marschall, H. R., et al. (2014). Development and evolution of detachment faulting along 50 km of the Mid-Atlantic Ridge near 16.5° N. *Geochemistry, Geophysics, Geosystems*, *15*(12), 4692–4711. https://doi.org/10.1002/2014gc005563

Soda, Y., Harigane, Y., Kajimoto, K., & Okudaira, T. (2019). Crystallographic preferred orientations of plagioclase via grain boundary sliding in a lower-crustal anorthositic ultra-mylonite. *International Journal of Earth Sciences*, *108*, 2057–2069. https://doi.org/10.1007/s00531-019-01749-z

Stipp, M., & Tullis, J. (2003). The recrystallized grain size piezometer for quartz. *Geophysical Research Letters*, *30*. https://doi.org/10.1029/2003GL018444

Svahnberg, H., & Piazolo, S. (2010). The initiation of strain localisation in plagioclase-rich rocks: Insights from detailed microstructural analyses. *Journal of Structural Geology*, *32*, 1404–1416. https://doi.org/10.1016/j.jsg.2010.06.011

Taufner, R., Viegas, G., Faleiros, F. M., Castellan, P., & Silva, R. (2021). Deformation mechanisms of granulite-facies mafic shear zones from hole U1473A, Atlantis Bank, Southwest Indian Ridge (IODP Expedition 360). *Journal of Structural Geology*, *149*, 104380. https://doi.org/10.1016/j.jsg.2021.104380

Twiss, R.J. (1977). Theory and applicability of a recrystallized grainsize paleopiezometer. *Pure and Applied Geophysics*, *115*, 27–244. https://doi.org/10.1007/bf01637105

Voigt, W. (1928). *Lehrbuch der Kristallphysik*. Leipzig: Teubner.

Walte, N. P., Bons, P. D., & Passchier, C. W. (2005). Deformation of melt-bearing systems: Insight from in situ grain-scale analogue experiments. *Journal of Structural Geology*, *27*(9), 1666–1679. https://doi.org/10.1016/j.jsg.2005.05.006

Zhao, N., Hirth, G., Cooper, R. F., Kruckenberg, S. C., & Cukjati, J. (2019). Low viscosity of mantle rocks linked to phase boundary sliding. *Earth and Planetary Science Letters*, *517*, 83–94. https://doi.org/10.1016/j.epsl.2019.04.019

## References From the Supporting Information

Bachmann, F., Hielscher, R., & Schaeben, H. (2010). Texture analysis with MTEX: Free and open source software toolbox. *Solid State Phenom*, *160*, 63–68. https://doi.org/10.4028/www.scientific.net/SSP.160.63

Boland, J. N., & Tullis, T. E. (1986). Deformation behaviour of wet and dry clinopyroxenite in the brittle to ductile transition region. In B. E. Hobbs, & H. C. Heard (Eds.), *Mineral and rock deformation: Laboratory studies, the Paterson volume, Geophysical monograph series* (pp. 35–49). Washington, D. C: AGU.

Dimanov, A., Jaoul, O., & Sautter, V. (1996). Calcium self-diffusion in natural diopside single crystals. *Geochim. Cosmochim. Acta*, *60*, 4095–4106.

Dimanov, A., Rybacki, E., Wirth, R., & Dresen, G. (2007). Creep and strain-dependent microstructure of synthetic anorthite-diopside aggregates. *Journal of Structural Geology*, *29*, 1049–1069.

Dimanov, A., & Sautter, V. (2000). “Average” interdiffusion of (Fe,Mn)-Mg in natural diopside. *European Journal of Mineralogy*, *12*, 749–760.

Farver, J.R., & Giletti, B.J. (1985). Oxygen diffusion in amphiboles. *Geochimica et Cosmochimica Acta*, *49*, 1403–1411.

Hacker, B. R., Abers, G. A., & Peacock, S. M. (2003). Subduction Factory. 1. Theoretical mineralogy, densities, seismic wave speeds, and $H_2O$ contents. *Journal of Geophysical Research*, *108*, B12029. https://doi.org/10.1029/2001JB001127

Hacker, B. R., & Christie, J. M. (1990). Brittle/ductile and Plastic/Cataclastic transitions in experimentally deformed and metamorphosed amphibolite. *Geophysical Monograph*, *56*, 127–147.

Hielscher, R., & Schaeben, H. (2008). A novel pole figure inversion method: Specification of the MTEX algorithm. *Journal of Applied Crystallography*, *41*, 1024–1037.

Hirth, G., & Kohlstedt, D. (2003). Rheology of the upper mantle and the mantle wedge: A view from the experimentalists. *Inside the subduction factory. Geophysical monograph* (pp. 83–105). American Geophysical Union. https://doi.org/10.1029/138GM06

Mainprice, D., Bachmann, F., Hielscher, R., & Schaeben, H. (2014). Descriptive tools for the analysis of texture projects with large datasets using MTEX: Strength, symmetry and components. *Geological Society, London, Special Publications*, *409*, 251–271. https://doi.org/10.1144/SP409.8

Olsen, T. S., & Kohlstedt, D. L. (1984). Analysis of dislocations in some naturally deformed plagioclase feldspars. *Physics and Chemistry of Minerals*, *11*, 153–160.

Papa, S., Pennacchioni, G., Menegon, L., & Thielmann, M. (2020). High stress creep preceding coseismic rupturing in amphibolite-facies ultramylonites. *Earth and Planetary Sciences Letters*, *541*, 116260.

Rybacki, E., Dresen, G. (2000). Dislocation and diffusion creep of synthetic anorthite aggregates. *Journal of Geophysical Research*, *105*(B11), 26017–26036.

Schroeder, T., & John, B.E. (2004). Strain localization on an oceanic detachment fault system, Atlantis Massif, 30°N, Mid-Atlantic Ridge. *Geochemistry, Geophysics, Geosystems*, *5*, 1–n. https://doi.org/10.1029/2004GC000728

Sneeringer, M., Hart, S. R., & Shimizu, N. (1984). Strontium and samarium diffusion in diopside. *Geochimica et Cosmochimica Acta*, *48*, 1589–1608.